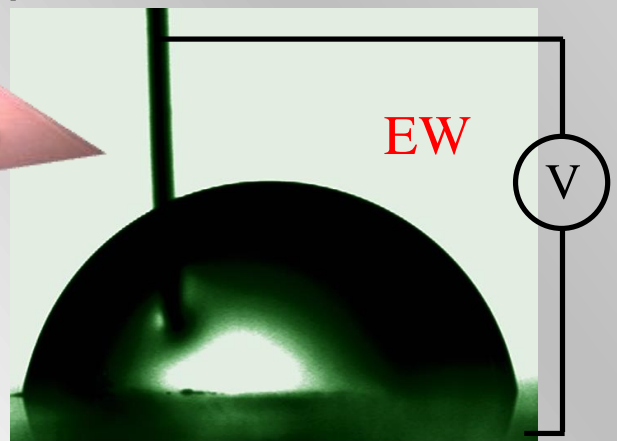
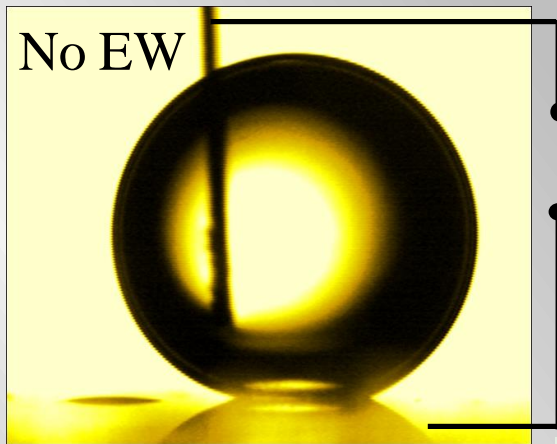


PHYSICS EDUCATION



**Basics and Applications of Electrowetting on
Dielectric**

Volume 30, Number 4**In this Issue**

- **Editorial** 01 page
Pramod Joag
- **Simulation of Earth orbit around Sun by Computational Method** 04 pages
Kumar and Prof. Y. C. Bhat
- **Relativistic Equations of Motion and the Newtonian Limit** 04 page
Mudit Jain
- **Transcending Three Dimensions in Physics** 09 pages
K. M. Udayanandan, R. K. Sathish , A. Augustine.
- **Damped Motion Of Electron In Electric Conduction Due to Presence Of Magnetic And Alternative Electric Fields At Right Angles And Closed Form** 08 pages
Soumendra Nath Maitra
- **Basics and Applications of Electrowetting on Dielectric** 15 Pages
Dineshkumar Y. Turkar, Sandip M. Wadhai, Yogesh B. Sawane, Arun G. Banpurkar
- **Piezoelectricity : A New Way of Taming Energy** 05 pages
Mukesh Kumar, Divakar Parashar
- **Magneto-caloric Effect and Magnetic Field Induced Strain of Heusler Alloys** 11 page
Mrittunjoy Guha Majumdar
- **Squaring and Cubing of Binary Numbers** 08 Pages
M. N. Murty
- **Physics Through Laboratory: Voltage Calibration Using Optical Method** 05 Pages
Rashmi P.E, Shivalingaswamy T. Raghu A.

EDITORIAL

It is a pleasure to publish the issue 30.4 of Physics Education. As you can see, this issue deals with variety of areas starting from computation of Earth's orbit, wetting of surfaces, piezoelectricity, magneto-caloric effect in alloys and so on. The feature "Physics Through lab" presents a novel optical method of voltage calibration. I am sure this issue will make an interesting reading for teachers and students alike.

Finally I wish all the readers of Physics Education a very happy and prosperous new year!

Pramod S. Joag.

Chief Editor, Physics Education

Chief-editor@physedu.in,

pramod@physics.unipune.ac.in

Simulation of Earth orbit around Sun by Computational Method

Pramod Kumar¹, Yogesh C. Bhatt², Yogendra S. Shishodiya³, Rajmal Jain⁴

^{1,2,3}Department of Physics
Jagan Nath University, Jaipur 303901, India.

²Jagan Nath Institute of Engineering and Technology, Jaipur 302022, India

⁴Kadi Sarwa Vishwavidhalaya, Gandhinagar India.

(Submitted 04-05-2014)

Abstract

Solar system is filled with many celestial bodies like planets, meteors, asteroids etc. Most of these bodies are rotating around the Sun. The study of orbital motions of the celestial bodies is important for astronomical point of view. In this paper the orbital motion of Earth is being simulated by using Kepler's Model of orbital Motion and Newton's Laws of motions. The simulation is achieved by using numerical method (Euler Cromer Method) and MATLAB software. Results show that varying time step in years and initial velocities of Earth motion, the Earth is getting unstable from its orbital motion.

1. Introduction

From the beginning of human civilizations, humans showed his great interest in exploring physical phenomenon and processes of the Earth and universe. Now, It is well known that the solar system consist Sun at its centre and having celestial bodies like planets, asteroids, meteors, comets etc. A planets move around Sun. Earth is the third planet after mercury and Venus from the Sun.

Studying orbital motions of celestial bodies have great importance in astrophysics. Earlier record shows that Nicolaus Copernicus was the first to develop an equation for a heliocentric system of Sun. Galileo Galilei, Johannes Kepler and Isaac Newton, (in the 17th Century) developed an understanding of physics that led to the gradual

acceptance of the idea that Earth moves around the physical laws that governed Earth [1].

The Earth orbit is the motion of Earth around Sun with an average distance 149.59787 million kilometers away. A complete orbit of the Earth around the Sun occurs every nearly in a one year. The orbital speed of the Earth around the Sun averages about 30 km/s which is fast enough to cover the planet's diameter (about 12,700 km) in seven minutes, and the distance to the Moon of 384,000 km in four hours [2].

Computer is now providing solutions in each field of work and study. The modeled physical processes and phenomenon can now be easily solved by numerical methods and using computers

[3]. Until 1950s the only methods used for obtaining numerical result lies on physical methods such as separation of variables, contour integration and conforming mapping [4]. Solving physical problems by Numerical methods have more advantages than analytical methods. Euler Cromer method, Newton Remption, Ruge Cutta Methods, Monte Carlo Methods and lot are major examples of numerical methods.

In this paper the simulation of the Earth orbit around Sun has been presented. Euler Cromer method [5] is used as a numerical technique and MATLAB is used for computation. The simulation of the orbital motion at different velocities and time steps is also analyzed. The obtained results are presented in the result section of the article.

2. Modeling and Computation

Orbit modeling is the process of creating mathematical models to simulate motion of a massive body as it moves in orbit around another massive body due to gravity. Earth orbit is modeled by using Kepler’s laws and Newton’s laws of Motion. These are discussed as follows:

A. Kepler’s laws are given by the following three statements:

- The planets move in elliptical orbits around the sun. The sun resides at one focus.
- The line joining the sun with any planet sweeps out equal areas in equal times.
- Given an orbit with a period T and a semi major axis a: the ratio T^2/a^3 is a constant.

B. Newton’s Second Law

Let us consider the motion of the Earth around the Sun. Let r be the distance and M_s and M_e be the masses of the Sun and the Earth respectively. After neglecting the effect of the Other planets and the motion of the Sun (i.e. we assume that $M_s \gg$

M_e). Our goal is to calculate the position of the Earth as a function of time

From the Newton’s Second law of motion

$$M_e \frac{d^2 \vec{r}}{dt^2} = - \frac{GM_e M_s}{r^3} \vec{r}$$

$$= - \frac{GM_e M_s}{r^3} (x\vec{i} + y\vec{j}) \dots\dots\dots 1$$

We get the two equations

$$\frac{d^2 x}{dt^2} = - \frac{GM_s}{r^3} x \dots\dots\dots 2$$

$$\frac{d^2 y}{dt^2} = - \frac{GM_s}{r^3} y \dots\dots\dots 3$$

We replace these two second-order differential equations by the four first-order differential equations

$$\frac{dx}{dt} = v_x \dots\dots\dots 4$$

$$\frac{dv_x}{dt} = - \frac{GM_s}{r^3} x \dots\dots\dots 5$$

$$\frac{dy}{dt} = v_y \dots\dots\dots 6$$

$$\frac{dv_y}{dt} = - \frac{GM_s}{r^3} y \dots\dots\dots 7$$

We recall

$$r = \sqrt{x^2 + y^2} \dots\dots\dots 8$$

C. Euler Cramer modeling of the Newton’s equation of motions is as follows:

The time discretization is

$$t \equiv t(i) = i\Delta t, i = 0, \dots\dots\dots, N \dots\dots\dots 9$$

The total time interval is $T = N\Delta t$. We define; $x(t) = x(i), v_x(t) = v_x(i), y(t) = y(i), v_y(t) = v_y(i)$.

Equations (4), (5), (6),(7) and (8) become for $i = 0, \dots\dots\dots, N$

$$v_x(i+1) = v_x(i) - \frac{GM_s}{(r(i))^3} \{x(i).\Delta t\} \dots\dots\dots 10$$

$$x(i+1) = x(i) + v_x(i) \Delta t \dots\dots\dots 11$$

$$v_y(i+1) = v_y(i) - \frac{GM_s}{(r(i))^3} \{y(i).\Delta t\} \dots\dots\dots 12$$

$$y(i+1) = y(i) + v_y(i) \Delta t. \dots\dots\dots 13$$

$$r(i) = \sqrt{x(i)^2 + y(i)^2} \dots\dots\dots 14$$

D. The MALAB code of Euler Cromer equations for simulation of orbital motion of Earth around Sun is given below for time step 0.002 in years and initial velocity 0 in AU/year. The initial position of planet is taken at 1 AU from the Sun.

```
>> npoints=500;
>> dt=0.002;

>> x=1;
>> y=0;
>> v_x=0;
>> v_y=2*pi;

>> plot(0,0,'oy','MarkerSize',30,'MarkerFaceColor',
'yellow');
>> axis([-1 1 -1 1]);
>> xlabel('x(AU)');
>> ylabel('y(AU)');
>> hold on;

>> for step=1:npoints-1;
radius=sqrt(x^2+y^2);
v_x_new=v_x-(4*pi^2*x*dt)/(radius^3);
v_y_new=v_y-(4*pi^2*y*dt)/(radius^3);
x_new=x+v_x_new*dt;
y_new=y+v_y_new*dt;
plot(x_new,y_new,'-k');
drawnow;
v_x=v_x_new;
```

```
v_y=v_y_new;
```

```
>> x=x_new;
```

```
>> y=y_new;
```

```
>> end;
```

3. Results and Discussions

The obtained result from the MATLAB simulation using following sets of values ($dt=0.002$, $V_Y=2*\pi$), ($dt=0.05$, $V_Y=2*\pi$), ($dt=0.05$, $V_Y=4$), ($dt=0.002$, $V_Y=4$) are shown in figures 1, 2, 3 and 4 respectively.

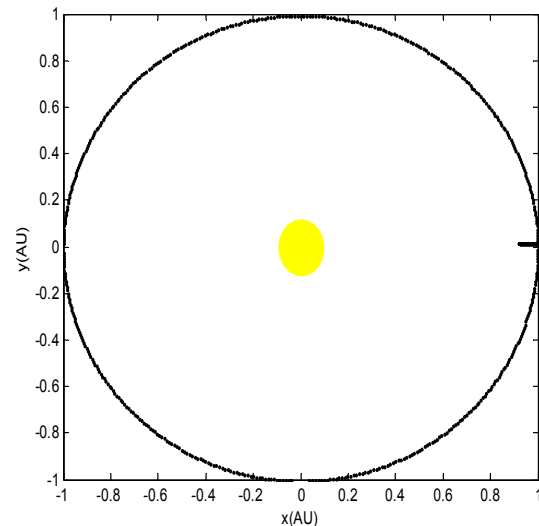


Fig. 1: Simulation of Earth Orbit around Sun ($dt=0.002$, $V_Y=2*\pi$)

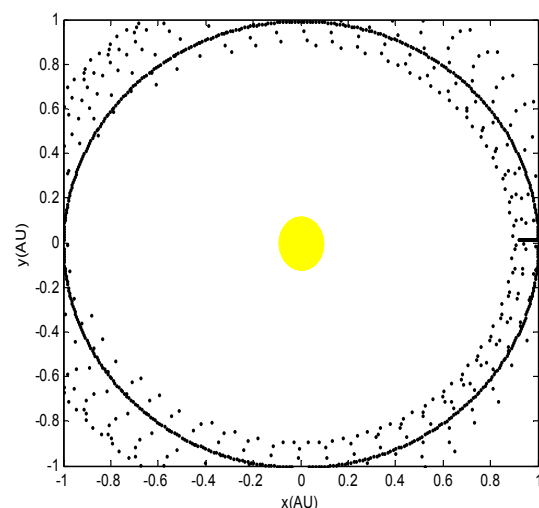


Fig. 2: Simulation of Earth Orbit around Sun ($dt=0.05$, $V_Y=2*\pi$)

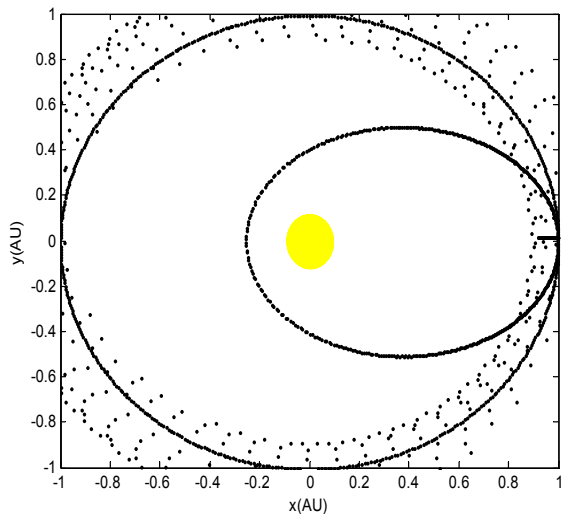


Fig. 3: Simulation of Earth Orbit around Sun ($dt=0.05$ $v_y=4$)

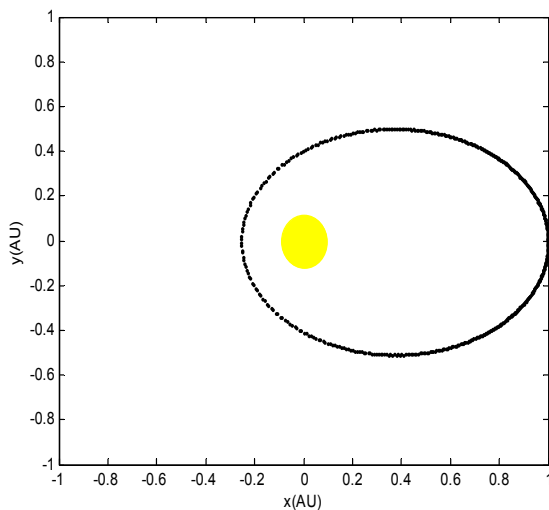


Fig. 4: Simulation of Earth Orbit around Sun ($dt=0.002$ and $v_y=4$)

The results are very significant as the value of time step increases from the 0.002 years. The orbital motion is unstable in case of 0.05 years. In figure 2 the time step is increased to 0.05 years which shows a clear unstable orbit of Earth. It is also visible in figure 3. While in figure 4 the stable orbit obtained with an increased velocity. This is in accordance with the rule of thumb that the time

step should be less than 1% of the characteristic time scale of the problem.

4. Conclusions

From the above simulation it is clear that varying time step the earth orbit get unstable. This is according to the rule of thumb that the time step should be less than 1% of the characteristic time scale of the problem.

Secondly computational methods have great advantage in simulating physical problems by using computer software and numerical methods.

Acknowledgements

Author wrote this paper for introduction purpose that how simulation work is useful in solving physical phenomenon by using numerical methods and computer. The authors thank to his Ph. D. supervisor Prof. Y. C. Bhatt (Former Prof. M/s MNIT Jaipur) for his guidance, encouragement and Prof. Rajmal Jain (former Prof. M/s PRL Ahmadabad) for his proper guidance and support.

References :

- [1] Weinert, Friedel *Copernicus, Darwin, & Freud: revolutions in the history and philosophy of science.*(Wiley-Blackwell, 2009). ISBN 978-1-4051-8183-9.
- [2] Williams, David R. "*Earth Fact Sheet*". (NASA. Retrieved 2007-03-17, 2004-09-01).
- [3] Leader, Jeffery J. *Numerical Analysis and Scientific Computation.* (Addison Wesley, 2004).. ISBN 0-201-73499-0.
- [4] C. D. Canterell, 2000, *Modern mathematical methods for physicist and engineers*, (Cambridge University Press, USA, 2000).
- [5] Martin Oliver Steinhauser, *Computer Simulation in Physics and Engineering*, (Walter de Gruyter, 2012). ISBN 3110256061, 9783110256062

Relativistic equations of motion and the Newtonian limit

Mudit Jain[†]

Department of Electrical Engineering
Jaipur Engineering College and Research Center
Rajasthan, India.
jain.mudit90@yahoo.com

[†]Current Affiliation: Department of Physics
University of Minnesota, Duluth
MN, US.
jainx286@d.umn.edu

(Submitted 11-10-2012)

Abstract

Working in an arbitrary inertial frame S , relativistic vector equations of motion of a particle for a constant acting force on it (as seen from S) are derived in cartesian coordintes following Newton's second law, and the equations are reduced to the well known kinematic Newtonian equations of motion under the non-relativistic limit.

1 Introduction

This article is dedicated to newcomers in special relativity and the aim is to derive the three vector equations of motion for a relativistic particle moving with instantaneous 3-velocity \mathbf{v} as observed by some inertial frame

S , and to rederive the famous kinematics equations by taking the non-relativistic limit which is $\lim c \rightarrow \infty$. The beginning point is Newton's second law: $\mathbf{F}_S = \frac{d\mathbf{p}}{dt}$, where \mathbf{p} and \mathbf{F}_S are the 3-momentum and the 3-force respectively as observed in frame S , and t is the coordinate time of S . The basic vector defi-

nitions of velocity \mathbf{v} and acceleration \mathbf{a} are taken as $\frac{d\mathbf{r}}{dt} = \dot{\mathbf{r}}$ and $\frac{d^2\mathbf{r}}{dt^2} = \ddot{\mathbf{r}}$ respectively, where \mathbf{r} and t are coordinate spatial separation vector and coordinate time respectively for the frame S. Some common terminology associated to relativistic mechanics is used and is assumed that the reader is aware of it.

The vector expression of relativistic 3-momentum for a massive particle, which can be obtained from the general lorentz transformations in minkowski space-time background[1-4], is given by

$$\mathbf{p} = \frac{m_o \mathbf{v}}{\sqrt{1 - \frac{\mathbf{v} \cdot \mathbf{v}}{c^2}}} \quad (1)$$

where m_o is the rest mass of the particle and \mathbf{v} is its 3-velocity, w.r.t S.

Assuming that a 3-force \mathbf{F}_S , as observed from S acts on the particle, Newton's second law gives,

$$\mathbf{F}_S = \frac{d}{dt} \frac{m_o \mathbf{v}}{\sqrt{1 - \frac{\mathbf{v} \cdot \mathbf{v}}{c^2}}} \quad (2)$$

Differentiating the above expression, one gets

$$\mathbf{F}_S = \frac{c^2 m_o \mathbf{a} + m_o \mathbf{v} \times \mathbf{a} \times \mathbf{v}}{c^2 \left(1 - \frac{\mathbf{v} \cdot \mathbf{v}}{c^2}\right)^{3/2}} \quad (3)$$

where $\mathbf{a} = d\mathbf{v}/dt$ is the 3-acceleration. As one can notice, the vector expression for acceleration of the particle acted upon by this force \mathbf{F}_S as seen from frame S is not a trivial one. However it is apparent that although

acceleration is absolute for different inertial frames (i.e. if it is zero in one inertial frame, it is zero in every other inertial frame), its value changes from one to another[2-4]. We now derive the relativistic equations of motion for the frame S, assuming that the 3-force \mathbf{F}_S is a constant.

2 Relativistic kinematic equations of motion

2.1 First

From (2) we have

$$\int d \frac{\mathbf{v}}{\sqrt{1 - \frac{\mathbf{v} \cdot \mathbf{v}}{c^2}}} = \frac{\mathbf{F}_S}{m_o} \int dt \quad (4)$$

which gives

$$\frac{\mathbf{v}}{\sqrt{1 - \frac{\mathbf{v} \cdot \mathbf{v}}{c^2}}} - \frac{\mathbf{u}}{\sqrt{1 - \frac{\mathbf{u} \cdot \mathbf{u}}{c^2}}} = \frac{\mathbf{F}_S}{m_o} (t - t_1) \quad (5)$$

on integration with the initial condition that at the instant $t = t_1$, the 3-velocity of the particle was \mathbf{u} . We set t_1 to zero. The equation can be elegantly written as

$$\mathbf{v}\gamma_v - \mathbf{u}\gamma_u = \frac{\mathbf{F}_S}{m_o} t \quad (6)$$

In the non-relativistic limit i.e. when $|\mathbf{u}|, |\mathbf{v}| \ll c$, it can be easily seen from (3) that acceleration is approximately a constant and is given by the expression $\mathbf{a} \approx \frac{\mathbf{F}_S}{m_o}$. From

this approximation, we obtain the first Newtonian equation of motion

$$\mathbf{v} - \mathbf{u} \approx \mathbf{a}t$$

2.2 Second

From equation (6), \mathbf{v} can easily be found to be equal to

$$\mathbf{v} = \frac{\mathbf{k}}{\sqrt{1 + \frac{\mathbf{k} \cdot \mathbf{k}}{c^2}}} \quad (8)$$

where $\mathbf{k} = \frac{\mathbf{F}_s}{m_o}t + \mathbf{u}\gamma_u$.

From $\int d\mathbf{r} = \int \mathbf{v}dt$ and the above expression for velocity, we get

$$\int d\mathbf{r} = \int \frac{\frac{\mathbf{F}_s t}{m_o} + \mathbf{u}\gamma_u}{\sqrt{1 + \left(\frac{\mathbf{F}_s t}{m_o c} + \frac{\mathbf{u}\gamma_u}{c}\right)^2}} dt \quad (9)$$

Although the integration is trivial, the answer is a mess:

$$\begin{aligned} \mathbf{r} = & \frac{c}{\sqrt{\mathbf{F}_s \cdot \mathbf{F}_s}} \left[\mathbf{F}_s \sqrt{(t + m_o A)^2 + B} \right. \\ & + m_o (\gamma_u \mathbf{u} - A \mathbf{F}_s) \ln \left(\frac{t + m_o A}{\sqrt{B}} \right. \\ & \left. \left. + \frac{\sqrt{(t + m_o A)^2 + B}}{\sqrt{B}} \right) + \mathbf{k}' \right] \end{aligned}$$

where

$$A = \frac{\mathbf{F}_s \cdot \mathbf{u}\gamma_u}{\mathbf{F}_s \cdot \mathbf{F}_s}; \quad B = m_o^2 \left(\frac{\gamma_u^2 c^2}{\mathbf{F}_s \cdot \mathbf{F}_s} - A^2 \right) \quad (10)$$

and \mathbf{k}' is a constant of integration found by plugging the initial separation vector as $\mathbf{r} = \mathbf{r}_1$ at $t = t_1$ which we have set to zero. This is the required second relativistic equation of motion and describes a hyperbola in the r, t space[5]. The non-relativistic limit gives us back the regular second kinematic equation of motion:

$$\mathbf{r} \approx \mathbf{r}_1 + \mathbf{u}t + \frac{\mathbf{a}}{2}t^2 \quad (11)$$

This describes a parabolic trajectory in the r, t space. The true hyperbolic trajectory has been approximated by a parabolic one in the non-relativistic limit.

2.3 Third

We begin with equation (2) and dot it with $d\mathbf{r}$ to give

$$d\mathbf{r} \cdot \frac{d}{dt} (\gamma_v \mathbf{v}) = \frac{1}{m_o} (\mathbf{F}_s \cdot d\mathbf{r}) \quad (12)$$

This is equivalent to

$$\mathbf{v} \cdot d(\gamma_v \mathbf{v}) = \frac{1}{m_o} (\mathbf{F}_s \cdot d\mathbf{r}) \quad (13)$$

For integration (note that it is a line integral), one can do integration by parts to get

$$|\gamma_v \mathbf{v} \cdot \mathbf{v}|_{boundary} - \int \gamma_v \mathbf{v} \cdot d\mathbf{v} = \frac{1}{m_o} \int \mathbf{F}_s \cdot d\mathbf{r} \quad (14)$$

Now the boundaries are of course the final and initial velocities (\mathbf{v} and \mathbf{u}) respectively for the left hand side and the final and initial positions (\mathbf{r} and \mathbf{r}_o) respectively for the right hand side. The second integral is trivial (note that $\mathbf{v} \cdot d\mathbf{v} = d(\mathbf{v} \cdot \mathbf{v})/2$) and the whole expression turns out to be

$$m_o c^2 (\gamma_v^2 - \gamma_u^2) = \mathbf{F}_s \cdot \Delta \mathbf{r} \quad (15)$$

where $\Delta \mathbf{r} = \mathbf{r} - \mathbf{r}_o$. Here too, one can easily get the Newtonian limit by taking $c \rightarrow \infty$:

$$2\mathbf{a} \cdot \mathbf{r} \approx \mathbf{v} - \mathbf{u} \quad (16)$$

which is the third non relativistic kinematic equation of motion.

3 Conclusion

These three relativistic equations of motions must be used when dealing with particles moving with velocities comparable to that of light. They can be efficiently reduced to Newtonian equations of motion when working with low velocities.

References

- [1] "Derivation of the relativistic momentum and relativistic equation of motion from Newton's second law and Minkowskian space-time geometry" ; Apeiron, Vol. 15, No. 3, July 2008
- [2] Misner C. W., Thorn K. S. and Wheeler J. A.: Gravitation, Freeman, San Francisco (1970).
- [3] R. M. Wald, General Relativity, University of Chicago Press, Chicago (1984).
- [4] Hobson M.P., Efstathiou G.P. and Lasenby A.N.: General Relativity: Cambridge University Press, New York (2006).
- [5] Herbert Goldstein, Charles P. Poole, John Safko : Classical Mechanics, Publisher: Pearson Education

Transcending three dimensions in physics

K. M. Udayanandan ^{1,a}, R. K. Sathish¹, A. Augustine. ²

¹ Department of Physics, Nehru Arts and Science College,
Kerala-671 314, INDIA,

²Former Visiting Professor, Department of Physics,
University of Kannur, Kerala 673 635, INDIA.

^audayanandan@gmail.com

(Submitted: 26-09-2014)

Abstract

We usually study or teach physics in the three dimensional or four dimensional space in classrooms. But now a days there is a growing interest among researchers [1-11] in multidimensional physics. In this article, we make a study of the Blackbody Radiation(BBR), Bose Einstein Condensation(BEC) and Pauli para magnetism in different dimensions. The reader can see that the study of physics is very much enjoyable with interesting surprises when we study some phenomena in higher or lower dimensions.

1 Introduction

The purpose of this article is to present three simple but interesting phenomena in statistical mechanics from the dimensional point of view. We organize the paper as follows. First we describe the Planck radiation law, Stefan Boltzmann law and Wien's law in d spatial dimensions and then discuss Bose Einstein condensation in arbitrary dimensions.

Finally we discuss Pauli para magnetism in three dimensions. Although some of these results about black body radiations are known in literature[1-6] we approach the derivations in a method as given in Pathria[3] which may be familiar to most of the students. BEC studies in different dimensions has been done earlier[7,8] but mainly it was done with massive bosons. We here study BEC with different energies in different dimensions. Pauli para magnetism in arbitrary dimensions has

also been reported[9] but we present here a simple method for its dimensional variation in 1, 2 and 3 dimensions. Nowadays it has become rather common to study the phenomena and underlying physics in arbitrary dimensions. The existence of extra dimensions has been a subject of intensive research study during the past few years [10-11]. The inclusion of extra dimensions plays a crucial role in many physical concepts, mostly in the construction of various models such as super string theory and general relativity [12-14]. The d dimensional dependence of physical laws would help us to understand their nature more profoundly and may give an answer to why our universe possesses three dimensions and not some other dimensions. Besides, from the point of view of physics education we can formulate various such simple problems in class rooms on higher dimensional physics which may stimulate the students' curiosity and imagination.

1.1 Planck's distribution law(PDL)

A black body cavity can be imagined to be filled with a gas of identical and indistinguishable quanta called photons with zero rest mass and with energy $E = \hbar\omega$. The energy of photons vary from 0 to infinity. Here we first analyze the blackbody radiation in a universe with 1, 2, 3 and d -spatial dimensions. Such a study was started by De Voss A in 1988[1] where no explicit expression for Stefan-Boltzmann constant in

d dimension was obtained. Later an exact derivation of Planck distribution law[PDL], Wien's displacement law and Stefan Boltzmann law were given by Peter T Landsberg and Alexis De Vos [2] based on principles of electrodynamic waves in cavities. In 2005 there were 2 papers[5] and [6] which also gives the same ideas from different point of view. We approach the derivation in a pedagogical way based on the phase space principles in statistical mechanics as given by Pathria[3]. Such a study will help the students directly study any multidimensional problem other than BBR. The number of micro states in phase space is given by

$$\Omega = \frac{\pi^{\frac{d}{2}} R^d L^d}{h^d \left(\frac{d}{2}\right)!}$$

Substituting $R = p = \frac{h\nu}{c}$ the number of states between ν and $\nu + d\nu$ is

$$g(\nu)d\nu = \frac{d\pi^{\frac{d}{2}} \nu^{d-1} L^d}{c^d \left(\frac{d}{2}\right)!}$$

Internal energy is given by

$$U = kT^2 \frac{\partial}{\partial T} \ln \mathcal{Z}$$

$$\ln \mathcal{Z} = -g_I \int_0^\infty g(\nu) d\nu \ln(1 - e^{-\beta h\nu})$$

where \mathcal{Z} is the grand partition function, $\beta = \frac{1}{kT}$ and g_I is the internal degree of freedom. Taking 2 internal degrees of freedom for photons

$$\frac{U}{L^d} = \int_0^\infty \frac{2d\pi^{\frac{d}{2}} h\nu^d}{c^d \left(\frac{d}{2}\right)!} \frac{1}{e^{\frac{h\nu}{kT}} - 1} d\nu$$

$$u(\nu)d\nu = \frac{2d\pi^{\frac{d}{2}}h\nu^d}{c^d(\frac{d}{2})!} \frac{1}{e^{\frac{h\nu}{kT}} - 1} d\nu$$

$$P \propto T^{d+1}$$

This is the PDL in d dimensions and we get Planck ' distribution functions as

$$u(\nu)d\nu = \frac{8\pi h\nu^3}{c^3} \frac{d\nu}{e^{\frac{h\nu}{kT}} - 1}$$

$$u(\nu)d\nu = \frac{4\pi h\nu^2}{c^2} \frac{d\nu}{e^{\frac{h\nu}{kT}} - 1}$$

$$u(\nu)d\nu = \frac{2h\nu}{c} \frac{d\nu}{e^{\frac{h\nu}{kT}} - 1}$$

Among the three first is the conventional Planck's distribution law in 3 dimensions and others are in 2 and 1 dimension respectively.

1.1.1 Thermodynamics of photon gas in d- dimensions

It is always informative to find the thermodynamics of photons and we do this here in different dimensions.

Pressure

We have

$$\ln \mathcal{Z} = -g_I \int_0^\infty g(\nu)d\nu \sum_{l=1}^\infty \frac{(-1)^l e^{-\beta h\nu l}}{l}$$

From[3] we know

$$\frac{PL^d}{kT} = \ln \mathcal{Z}$$

On integrating we get

$$P = \frac{2d!\pi^{\frac{d}{2}}}{(\frac{d}{2})!} \frac{k^{(d+1)}T^{(d+1)}}{c^d h^d} \sum_{l=1}^\infty \frac{1}{l^{d+1}}$$

$$S \propto L^d T^d$$

which is Stefan-Boltzmann law in d dimensions.

Energy density

Using the equation for energy we get

$$\frac{U}{L^d} = \frac{2d!\pi^{\frac{d}{2}}}{(\frac{d}{2})!} \frac{k^{d+1}T^{d+1}}{c^d h^d} \sum_{l=1}^\infty \frac{1}{l^{d+1}} \quad (1)$$

$$U \propto T^{d+1}$$

Then the relationship between the pressure and energy density for a photon gas is

$$P = \frac{1}{d} \frac{U}{L^d}$$

For 3 dimensions we get $P = \frac{1}{3} \frac{U}{V}$

Entropy

Using the relation $A = U - TS$, where A is the Helmholtz free energy, S is the entropy and with $A = -kT \ln \mathcal{Z}$ (since chemical potential of photon gas is zero) we get

$$S = \left(1 + \frac{1}{d}\right) \frac{2dd!\pi^{\frac{d}{2}}}{(\frac{d}{2})!} \frac{k^{d+1}T^d}{c^d h^d} L^d \sum_{l=1}^\infty \frac{1}{l^{d+1}}$$

1.1.2 Wien’s displacement law

PDL curve rises and become a maximum and then decreases and there is a $\lambda = \lambda_{max}$ for which intensity is a maximum. From the distribution law for frequency, using $c = \nu\lambda$ we get

$$u(\lambda)d\lambda = \frac{-2d\pi^{\frac{d}{2}}hc}{\lambda^{d+2}(\frac{d}{2})!} \frac{1}{e^{\frac{hc}{\lambda kT}} - 1} d\lambda$$

When $\lambda = \lambda_{max}$,

$$\frac{du(\lambda)}{d\lambda} = 0$$

we get

$$\frac{xe^x}{e^x - 1} = d + 2$$

where $x = \frac{hc}{\lambda_{max}kT}$. This is a transcendental equation for whom some solutions are

$$x_1 = 2.8214$$

$$x_2 = 3.9207$$

$$x_3 = 4.9651$$

$$x_4 = 5.9849$$

$$x_5 = 6.9936$$

In 3 D

$$\frac{xe^x}{e^x - 1} = 5$$

Using these equations we can show that the color of the sun with surface temperature 6000 K will be yellow in 3 dimensions, near red in 2 dimensions and infra red in 1 dimension.

1.1.3 Stefan Boltzmann law

This law was deduced from experimental observation by Stefan in 1879; five years later Boltzmann derived it from thermodynamic consideration. The energy radiated per unit area per unit time is related to energy density of the body as[2],

$$R = \frac{U}{L^d} R^d$$

where

$$R^d = c \frac{\Gamma(\frac{d}{2})}{2\sqrt{\pi}\Gamma(\frac{(d+1)}{2})}$$

Substituting the value of U we get

$$R = \sigma_d T^{d+1} \tag{2}$$

where d dimensional Stefan- Boltzmann constant is

$$\sigma_d = \frac{2\pi^{\frac{d-1}{2}}}{\Gamma(\frac{(d+1)}{2})} \frac{\Gamma(d+1)\zeta(d+1)}{h^d c^{d-1}} R^{d+1}$$

Equation[2] is the d dimensional Stefan Boltzmann law. In 3 D

$$\sigma_3 = 5.67 \times 10^{-8} Wm^{-2}K^{-4}$$

In 2 D

$$\sigma_2 = 1.92 \times 10^{-10} Wm^{-1}K^{-3}$$

In 1 D

$$\sigma_1 = 9.46 \times 10^{-13} WK^{-2}$$

These equations show that σ is a dimensional dependent constant. The 1 D equation expresses the thermal noise power transfer in

one-dimensional optical systems and we get a similar equation for Johnson noise or Nyquist noise[2]. As already indicated in the abstract we can see some interesting and surprising results like the dimensional dependence of the color of the sun, dimensional dependence of Stefan Boltzmann constant etc.

2 Some Low dimensional problems

2.1 Bose Einstein Condensation

Now we consider another topic BEC which is now an active research problem. All the particles in nature may be classified as either bosons or fermions according to the value of their spin angular momentum. Particles with integer spin are bosons and particles with half integer spin are called fermions. Most of the fundamental building blocks of matter (e.g. electrons, neutrons, and protons) are fermions. A composite particle comprising an even number of fermionic building blocks (such as an atom) are also bosons and with odd number are fermions. The wave function describing the state of a system of particles will be symmetric for bosons and anti symmetric for fermions. The properties of ultra-cold atomic gases are dramatically different for bosons and fermions. Below a critical temperature, bosons undergo a phase transition and a macroscopic number of the atoms are forced into the lowest energy state of the

system. This phenomenon is called Bose Einstein Condensation. Simply speaking Bose Einstein Condensation is the piling up of particles in the lowest energy level, below a particular temperature called critical temperature. We can see that equations for BEC is different for different energies.

2.1.1 Massive non relativistic bosons

Consider a gas of bosons with energy $\frac{p^2}{2m}$ where p is the momentum and m is the mass of the particle.

Three Dimension

In grand canonical formulation

$$\ln \mathcal{Z} = -g_I \sum_p \ln (1 - ze^{-\beta \varepsilon_p})$$

where ε_p is a function of p . Here \mathcal{Z} is the grand partition function z is the fugacity which is related to the chemical potential μ as $z = e^{\beta \mu}$ and g_I is the internal degree of freedom which is 1 for a classical particle. Taking all these

$$\ln \mathcal{Z} = - \sum_p \ln \left(1 - ze^{-\beta \frac{p^2}{2m}} \right)$$

On simplifying using the number of states between p and $p + dp$ as $g(p)dp = \frac{4\pi p^2 dp V}{h^3}$ we get

$$\ln \mathcal{Z} = g_{\frac{5}{2}}(z) \frac{V}{\lambda^3} \quad (3)$$

where $g_{\frac{3}{2}}(z) = \sum_{l=1}^{\infty} \frac{z^l}{l^{\frac{3}{2}}}$ and thermal De Broglie wavelength $\lambda = \frac{h}{(2\pi mkT)^{\frac{1}{2}}}$. Here k is Boltzmann constant.

The total number of bosons in a given state can be obtained by using the expression

$$N = z \frac{\partial}{\partial z} \ln \mathcal{Z} \tag{4}$$

$$N = \frac{V}{\lambda^3} g_{\frac{3}{2}}(z)$$

For the Bose particles there is no restriction on the number of particles to occupy any level in the system. Let N_0 be the number of particles in the ground state. For temperature very much greater than critical temperature, the number of particles in the ground state will be very very small. Hence we can write

$$N = \frac{V}{\lambda^3} g_{\frac{3}{2}}(z) + N_0$$

at $T = T_c$, $z = 1$ [3] $V = \frac{N\lambda_c^3}{g_{\frac{3}{2}}(1)}$

Substituting this in the equation for N we get,

$$\frac{N_0}{N} = 1 - \left(\frac{T}{T_c}\right)^3$$

This is the equation of BEC. The right hand side of the equation is the fraction of total number of particles in the ground state. We can see that at $T = T_c$, $N_0 = 0$ which means no particle in the ground state. When $T < T_c$, $N \approx N_0$, which means the significant fraction of total number of particles are in the lowest possible energy state. When $T = 0$, $N = N_0$ all the particles are in the

ground state which is BEC. Now this curious phenomenon can be done in 2 and 1 dimensions.

Two and one Dimension

For 2 dimensions we will get $\ln \mathcal{Z} = \frac{A}{\lambda^2} g_2(z)$ and $N = \frac{A}{\lambda^2} g_1(z) = \frac{A}{\lambda^2} \zeta(1)$. For one dimension we will get $\ln \mathcal{Z} = \frac{L}{\lambda} g_{\frac{3}{2}}(z)$, $N = \frac{L}{\lambda} g_{\frac{3}{2}}(1) = \frac{L}{\lambda} \zeta(\frac{1}{2})$ for $\mu = 0$. The expressions for N are non physical or the condensation for massive bosons in 2D and 1-D does not occur.

BEC for bosons with relativistic massless and harmonic oscillator energy

For massless relativistic, identical, non-interacting bosons the energy is given by $\epsilon = c|p|$. Using the number of states as for massive bosons we get $\ln \mathcal{Z} = \left(\frac{V}{\lambda^3}\right) g_4(z)$

where $g_4(z) = \sum_{l=1}^{\infty} \frac{z^l}{l^4}$ and $\lambda = \frac{hc}{2\pi^{\frac{1}{3}} mkT}$. Then

$N = \left(\frac{V}{\lambda^3}\right) g_3(z) = \left(\frac{V}{\lambda^3}\right) \zeta(3)$ which has definite value and hence condensation is possible. For 2 dimensions $\ln \mathcal{Z} = \left(\frac{A}{\lambda^2}\right) g_3(z)$. With this $N = \left(\frac{A}{\lambda^2}\right) g_2(z) = \left(\frac{A}{\lambda^2}\right) \zeta(2)$ which has once again definite value. This result shows that massless bosons in 2D do indeed form a condensate. But for one dimension $N = \left(\frac{L}{\lambda}\right) \zeta(1) \rightarrow \infty$ which forbids condensation. For harmonic potential energy Hamiltonian is of the form $H = \frac{p^2}{2m} + \frac{1}{2}m\omega^2 r^2$ Using this Hamiltonian as above we can show

that BEC is possible in 3 and 2 dimensions= for 2 dimensions and
and not possible in in 1 dimension.

2.2 Pauli Para magnetism

Pauli para magnetism arises due to the alignment of the spin magnetic moments of free electrons. Here we consider low temperature (absolute zero), low field para magnetism of metals or free electron gas. We assume that the electrons with dipole moment μ will be either parallel to the field B or anti parallel. We thus have two groups of particles in the gas:

1. Electrons having μ parallel to B, with energy $\frac{p^2}{2m} - \mu B$
2. Electrons having μ anti-parallel to B, with energy $\frac{p^2}{2m} + \mu B$

At absolute zero, all energy levels up to the Fermi level ϵ_F will be filled, while all levels beyond ϵ_F will be empty. Accordingly, the kinetic energy of the particles in the first group will range between 0 and $(\epsilon_F + \mu B)$, while the kinetic energy of the particles in the second group will range between 0 and $(\epsilon_F - \mu B)$. The respective numbers of particles in the two groups will, therefore, be equal to the number of levels and then will be equal to

$$N^+ = \frac{4\pi V}{3h^3} (p_F^+)^3; N^- = \frac{4\pi V}{3h^3} (p_F^-)^3$$

for 3 dimensions

$$N^+ = \frac{\pi A}{h^2} (p_F^+)^2; N^- = \frac{\pi A}{h^2} (p_F^-)^2$$

$$N^+ = \frac{L}{h} p_F^+; N^- = \frac{L}{h} p_F^-$$

for 1 dimension where $p_F^+ = [2m(\epsilon_F + \mu B)]^{\frac{1}{2}}$, $p_F^- = [2m(\epsilon_F - \mu B)]^{\frac{1}{2}}$, V is the volume, A is the area and L is the length of the material. The intensity of magnetization $M = \mu(N^+ - N^-)$ and using the expression for susceptibility $\chi = \lim_{B \rightarrow 0} \frac{M}{B}$ we get

$$\chi_{3D} = C_1 (\epsilon_F)^{\frac{1}{2}}$$

$$\chi_{2D} = C_2$$

$$\chi_{1D} = C_3 (\epsilon_F)^{-\frac{1}{2}}$$

We can see that at low magnetic field and at absolute zero Kelvin, Pauli para magnetism in 2 dimension is a constant independent of Fermi temperature which indicates that it is independent of the material which is indeed a curious result demanding more investigations on para magnetism.

2.3 Conclusions

In Coulombs law the factor $4\pi r^2$ comes because of the 3 dimensional nature. For all spherical or 3 D variation this term will be there. If we express Coulomb's law in other dimensions what will be its nature is not always discussed in regular class rooms or the dimensionality dependences in the fundamental laws of physics are not described in most of the textbooks. Maxwell equations, Lorentz force, Coulomb law, the Schroedinger equation and Newton law of universal gravitation

in d spatial dimensions were obtained[4] by Masaki Hayashi and Kazuo Katsuura. One can recognize how the dimensionality of the world is reflected in these equations and laws. One problem that exists is the visualization of the extra dimensions. If extra dimensions exist, either they must be hidden from us by some physical mechanism or we do not have proper techniques to identify them. Studies point out a possibility that the extra dimensions may be "curled up" and hence invisible.

Acknowledgment

One of the authors Dr. K. M. Udayanandan wish to acknowledge Prof Subodh R Shenoy, TIFR Center for Interdisciplinary Sciences, Hyderabad for useful discussions.

References

1. De Vos A, Thermodynamics of radiation energy conversion in one and in three physical dimensions, *Phys. Chem. Solids*, 49, 725-30(1988)
2. Peter T Lands berg and Alexis De Vos, The Stefan-Boltzmann constant in n -dimensional space , *J. Phys. A: Math. Gen.* 22 (1989) 1073-1084.
3. R. K. Pathria and Paul D. Beale, *Statistical Mechanics*.(Third Edition-1996), Butter worth.
4. Masaki Hayashi and Kazuo Katsuura, On spatial dimensions in physical laws, *Revi.da Mexicana de Fsica*, 37 No. 4 (1991) 112-119
5. Tatiana R. Cardoso and Antonio S. de Castro, The blackbody radiation in a D -dimensional universes, *Revista Brasileira de Ensino de Fsica*, v. 27, No. 4, p. 559 - 563, (2005)
6. Hvard Alnes, Finn Ravndal and Ingunn Kathrine Wehus, Black-body radiation with extra dimensions, *J. Phys. A: Math. Theor.* 40 (2007) 1430914316
7. Ajanta Bhowal Acharyya and Mukdish Acharyya, Bose Einstein Condensation in arbitrary dimensions, No 9, Vol. 43 (2012), *Actaphysicapolonica B*.
8. Sami Al- Jaber, Ideal Bose Gas in Higher Dimensions, *An - Najah Univ. J. Res. (N. Sc.)* Vol. 22, 2008.
9. M. Acharyya, Pauli spin para magnetism and electronic specific heat in generalized d dimensions, *Commun. Theor. Phys.* 55 (2011) 901
10. Csaki, C. (2004) TASI Lectures on Extra dimensions and Branes. hep,ph 0404096.
11. Sundrum, R. (2005) To the Fifth Dimension and Back. TASI.
12. Green, M.B., Schwarz, J.H. and Witten, E. (1987) *Super string Theory*. University Press, Cambridge.
13. Brink, L. and Henneaux, M. (1988) *Principles of String Theory*. Plenum Press, New York.

14. Carroll, S.M. (1997) Lecture Notes on General Relativity. University of California, Oakland.

Damped Motion of Electron in Electric Conductor Due Presence of Magnetic and Alternative Electric Fields at Right Angles and Closed form Solutions

S. N. Maitra

Flat 303, Elite Galaxy,
Ram Nagar Colony,
N. D. A.- Pashan Road,
Bavdhan, Pune- 411021

Email: soumen_maitra@yahoo.co.in

(Submitted: 01-10-2014)

Abstract

Flow of current in an electric conductor is attributed to movement of electrons in the opposite directions. In this paper a second- order differential equation of an electron is formed taking into account ¹ a damping force owing to collisions between electrons and two more applied forces, magnetic field and alternative electric field in perpendicular directions and has been completely solved in closed form subject to the prescribed initial conditions. The governing differential equation of motion of the electrons is separated into two tractable simultaneous equations by use of complex number i ($I = \sqrt{-1}$). It is proved that the effect of damping partially dies away after sometime vis-à-vis theoretically after a long time, say after infinite time. The acceleration, velocity and distance described by the electron at any instant of time are determined. Thereafter their maximum and minimum values are found out.

1. Introduction

Mahindra Sing Sodha published a paper in Aug 07 issue of Bull IAPT wherein he has considered damped motion of an electron with formation of its relevant differential equation of motion in three cases but without going in for solution to the last case. “For presentation in 27th IAPT annual convention, Cochin University, Nov 02-04-2012.”

To, Dr. P. Radhakrishnan Email: radhak@cusat.ac.in”.

1. When the damped force acting on the electron is proportional to its velocity
2. When an electric field of constant magnitude is coupled with the damping force.
3. When the electron is acted on by three forces altogether, magnetic and electric fields of constant magnitudes at right angles and the damping force.

Sodha¹, however, examined its motion reaching the steady state and the heating effects together with current density are also discussed by him S. N. Maitra² solved the relevant differential equation of motion of an electron in presence of damping force and two mutually perpendicular magnetic and electric fields of constant magnitudes with a subtle technique of a complex number i ($i = \sqrt{-1}$) subject to given initial conditions and subsequently explained the reasons for the

electron attaining the steady state wherein the acceleration disappears. F acceleration acquired by the electron at any instant of time and the corresponding distance described by it. Nonetheless, in the present paper the entire problem vis-à-vis the third case is modified in a more cumbersome manner introducing an alternative electric field instead of electric field with constant magnitude and is ultimately solved in closed form.

1. Differential equation of motion

Let $\vec{r} = ix + jy$ and $\vec{v} = Iv_x + jv_y$ be the position and velocity vectors of an electron of mass m with charge e at any instant of time t with respect to a fixed frame OXY with origin at O and i, j as unit vectors along axes OX and OY at right angles, respectively. The electron moves under the following forces: Alternative electric Field

$$\vec{Electric\ Field} = \vec{E} \cos \omega_0 t = (IE_x + j E_y) \dots\dots\dots(1)$$

Magnetic field perpendicular to the electric field of magnitude B,

$$\vec{B} = \hat{k} B \dots\dots\dots(2)$$

Where, \hat{k} = unit vector perpendicular to i, j and damping force.

$$\vec{F} = mk\vec{v} \dots\dots\dots(3)$$

With constant damping factor k , \hat{k} = unit vector perpendicular to I , j . Hence in view of (1) to (3), the vector equation governing the motion of the electron is

$$m \frac{d\bar{v}}{dt} + mk\bar{v} = -e [\bar{E} \cos w_0 t + \bar{v} \times \bar{B}] \dots (4)$$

$$\bar{v} = \frac{d\bar{r}}{dt} \dots \dots \dots (5)$$

Which, can be rewritten in scalar form

$$I \frac{dV_x}{dt} + j \frac{dV_y}{dt} + k(iV_x + jV_y) = -\frac{e}{m} [IE_x + jE_y] \cos w_0 t + (IV_x + jV_y) \times \hat{k} B \dots \dots \dots (6)$$

Equating the coefficients of I and j from both side (6),

$$\dot{V}_x + kV_x = -a_x \cos w_0 t - wV_y, \quad \dot{V}_y + kV_y = -a_y \cos w_0 t - wV_x \dots \dots \dots (7)$$

Or

$$\dot{V}_x + kV_x + wV_y = -a_x \cos w_0 t \dots \dots \dots (8)$$

$$\dot{V}_y + kV_y - wV_x = -a_y \cos w_0 t \dots \dots \dots (9)$$

Where some constant parameters involved are

$$a_x = \frac{eE_x}{m}, a_y = \frac{eE_y}{m}, w = \frac{eB}{m} \dots \dots \dots (10)$$

And the dot sign derivatives with respect to time t .

2. Complete solution to motion of the Electron.

Multiplying equation (9) by $(I = \sqrt{-1})$ and thereafter adding to and subtracting from (8) we get two linear equations i.e. first order differential equations

$$(V_x + IV_y)^0 + (k - Iw)(V_x + IV_y) = -(a_x + Ia_y) (\cos w_0 t) \dots \dots \dots (11)$$

$$(V_x - IV_y)^0 + (k + Iw)(V_x - IV_y) = -(a_x - Ia_y) (\cos w_0 t) \dots \dots \dots (12)$$

It can be noted that (12) can be obtained by replacing I by $-I$ in (11)

Let us introduce the initial conditions that at $t=0$, $x=0$, $y=0$, $V_x = 0$ and $V_y = 0 \dots \dots \dots (13)$

this, means that the electron starts from the origin at rest and is accelerated owing to the applied electric and magnetic fields;

In order to solve (11) we find its integrating factor

$$L = e^{(k-Iw)t}$$

So that

$$e^{(k-Iw)t} \frac{d}{dt} (V_x + IV_y) + (k - Iw)(V_x + IV_y)e^{(k-Iw)t} = -(a_x + Ia_y)e^{(k-Iw)t} \cos w_0 t$$

Or

$$\frac{d}{dt} \{ (V_x + IV_y) e^{(k-Iw)t} \} = \frac{1}{2} (a_x + Ia_y) (e^{Iw_0 t} + e^{-Iw_0 t}) \dots\dots\dots(14)$$

Therefore;

$$e^{\pm Iw_0 t} = \cos w_0 t \pm I \sin w_0 t$$

$$\cos w_0 t = \frac{1}{2} (e^{Iw_0 t} + e^{-Iw_0 t})$$

$$\sin w_0 t = \frac{1}{2I} (e^{Iw_0 t} - e^{-Iw_0 t}) \dots\dots\dots(15)$$

Integrating (1) subject to the conditions (13), once gets

$$\begin{aligned} & \{V_x + IV_y\} e^{(k-Iw)t} \\ &= -\frac{1}{2} (a_x + Ia_y) \int_0^t e^{\{k+I(w_0-w)\}t} \\ &+ e^{\{k-I(w_0+w)\}t} dt \end{aligned}$$

$$V_x + IV_y = -\frac{1}{2} (a_x + Ia_y)$$

$$\begin{aligned} & \left[\frac{e^{Iw_0 t} \{k - I(w_0 - w)\}}{k^2 + (w_0 - w)^2} \right. \\ &+ \frac{e^{-Iw_0 t} \{k + I(w_0 + w)\}}{k^2 + (w_0 + w)^2} \\ &- \left. \frac{k - I(w_0 - w)}{k^2 + (w_0 - w)^2} \right. \\ &+ \left. \frac{k + I(w_0 + w)}{k^2 + (w_0 + w)^2} \right] e^{-\{k-Iw\}t} \end{aligned}$$

By use of (15)

$$V_x + IV_y = -\frac{1}{2} (a_x + Ia_y)$$

$$\begin{aligned} & \left[(k \cos w_0 t) \left\{ \frac{1}{k^2 + (w_0 - w)^2} + \frac{1}{k^2 + (w_0 + w)^2} \right\} + \right. \\ & (\sin w_0 t) \left\{ \frac{-(w_0 - w)}{k^2 + (w_0 - w)^2} + \frac{(w_0 + w)}{k^2 + (w_0 + w)^2} \right\} + \\ & I \left\{ \frac{-(w_0 - w) (\cos w_0 t)}{k^2 + (w_0 - w)^2} + \frac{(w_0 + w) (\cos w_0 t)}{k^2 + (w_0 + w)^2} + \right. \\ & \left. \frac{k \sin w_0 t}{k^2 + (w_0 - w)^2} - \frac{k \sin w_0 t}{k^2 + (w_0 + w)^2} \right\} - e^{-kt} \left\{ \frac{k \cos w_0 t}{k^2 + (w_0 - w)^2} + \right. \\ & \left. \frac{k \cos w_0 t}{k^2 + (w_0 + w)^2} - \frac{(w_0 - w) \sin w_0 t}{k^2 + (w_0 - w)^2} - \frac{(w_0 + w) \sin w_0 t}{k^2 + (w_0 + w)^2} \right\} - \\ & I \left\{ \frac{(w_0 + w) \cos wt}{k^2 + (w_0 - w)^2} - \frac{(w_0 - w) \cos wt}{k^2 + (w_0 + w)^2} + \frac{k \sin wt}{k^2 + (w_0 - w)^2} + \right. \\ & \left. \frac{k \sin wt}{k^2 + (w_0 + w)^2} \right\} \dots\dots\dots(16) \end{aligned}$$

Wherefrom equating the real and imaginary parts we get components of the electron along X and Y axes respectively.

$$\frac{dx}{dt} = V_x = \frac{a_y}{2} \left[\frac{(w_0+w) \cos w_0 t - k \sin w_0 t}{k^2 + (w_0+w)^2} + \frac{(w_0-w) \cos w_0 t + k \sin w_0 t}{k^2 + (w_0-w)^2} \right] - \frac{a_x}{2} \left\{ \frac{(w_0+w) \sin w_0 t - k \cos w_0 t}{k^2 + (w_0+w)^2} - \frac{(w_0-w) \sin w_0 t - k \cos w_0 t}{k^2 + (w_0-w)^2} \right\} - e^{-kt} \left[\frac{a_x}{2} \left\{ \frac{k \cos wt - (w_0+w) \sin wt}{k^2 + (w_0+w)^2} + \frac{k \cos wt - (-w_0+w) \sin wt}{k^2 + (w_0-w)^2} - \frac{a_y}{2} \left\{ \frac{k \sin wt + (w_0+w) \cos wt}{k^2 + (w_0+w)^2} + \frac{k \sin wt + (-w_0+w) \cos wt}{k^2 + (w_0-w)^2} \right\} \right] \dots\dots\dots(17)$$

$$\frac{dy}{dt} = V_y = -\frac{a_y}{2} \left[\frac{(w_0+w) \sin w_0 t + k \cos w_0 t}{k^2 + (w_0+w)^2} + \frac{k \cos w_0 t + (w_0-w) \sin w_0 t}{k^2 + (w_0-w)^2} \right] - \frac{a_x}{2} \left\{ \frac{(w_0+w) \cos w_0 t - k \sin w_0 t}{k^2 + (w_0+w)^2} - \frac{(w_0-w) \cos w_0 t - k \sin w_0 t}{k^2 + (w_0-w)^2} \right\} - e^{-kt} \left[\frac{a_y}{2} \left\{ \frac{k \cos wt - (w_0+w) \sin wt}{k^2 + (w_0+w)^2} + \frac{k \cos wt - (-w_0+w) \sin wt}{k^2 + (w_0-w)^2} + \frac{a_x}{2} \left\{ \frac{k \sin wt + (w_0+w) \cos wt}{k^2 + (w_0+w)^2} + \frac{k \sin wt + (-w_0+w) \cos wt}{k^2 + (w_0-w)^2} \right\} \right] \dots\dots\dots(18)$$

Integrating (17) and (18) and applying the initial conditions, we obtain the distance travelled by the electron along the axis:

$$x = \frac{a_y}{2} \left[\frac{(1+\frac{w}{w_0}) \sin w_0 t - (\frac{k}{w_0})(1-\cos w_0 t)}{k^2 + (w_0+w)^2} + \frac{(\frac{w}{w_0}-1) \sin w_0 t + (\frac{k}{w_0})(1-\cos w_0 t)}{k^2 + (w_0-w)^2} \right] - \frac{a_x}{2} \left\{ \frac{(1+\frac{w}{w_0})(1-\cos w_0 t) + (\frac{k}{w_0}) \sin w_0 t}{k^2 + (w_0+w)^2} + \dots\dots\dots(19)$$

$$\left. \frac{(\frac{w}{w_0}-1)(1-\cos w_0 t) - (\frac{k}{w_0}) \sin w_0 t}{k^2 + (w_0-w)^2} \right\} + e^{-kt} \left[\frac{a_x}{2} \left\{ \frac{k\{k[(1-\cos wt) + w \sin wt] - (w_0+w)[w(1-\cos wt) - k \sin wt]\}}{\{k^2 + (w_0+w)^2\}(k^2 + w^2)} - \frac{k\{k[(1-\cos wt) + w \sin wt] - (w-w_0)[w(1-\cos wt) - k \sin wt]\}}{\{k^2 + (w_0-w)^2\}(k^2 + w^2)} \right\} - \frac{a_y}{2} \left\{ \frac{k\{w[(1-\cos wt) - k \sin wt] + (w_0+w)[k(1-\cos wt) + w \sin wt]\}}{\{k^2 + (w_0+w)^2\}(k^2 + w^2)} + \frac{k\{w[(1-\cos wt) - k \sin wt] + (w-w_0)[k(1-\cos wt) + w \sin wt]\}}{\{k^2 + (w_0-w)^2\}(k^2 + w^2)} \right\} \right] \dots\dots\dots(19)$$

$$y = -\frac{a_y}{2} \left[\frac{(1+\frac{w}{w_0})(1-\cos w_0 t) + (\frac{k}{w_0}) \sin w_0 t}{k^2 + (w_0+w)^2} + \frac{(\frac{k}{w_0}) \sin w_0 t - (\frac{w}{w_0}-1)(1-\cos w_0 t)}{k^2 + (w_0-w)^2} \right] - \frac{a_x}{2} \left\{ \frac{(1+\frac{w}{w_0}) \sin w_0 t - (\frac{k}{w_0})(1-\cos w_0 t)}{k^2 + (w_0+w)^2} + \frac{(\frac{w}{w_0}-1) \sin w_0 t + (\frac{k}{w_0})(1-\cos w_0 t)}{k^2 + (w_0-w)^2} \right\} + e^{-kt} \left[\frac{a_y}{2} \left\{ \frac{k\{k[(1-\cos wt) + w \sin wt] - (w_0+w)[w(1-\cos wt) - k \sin wt]\}}{\{k^2 + (w_0+w)^2\}(k^2 + w^2)} - \frac{k\{k[(1-\cos wt) + w \sin wt] - (w-w_0)[w(1-\cos wt) - k \sin wt]\}}{\{k^2 + (w_0-w)^2\}(k^2 + w^2)} \right\} + \frac{a_x}{2} \left\{ \frac{k\{w[(1-\cos wt) - k \sin wt] + (w_0+w)[k(1-\cos wt) + w \sin wt]\}}{\{k^2 + (w_0+w)^2\}(k^2 + w^2)} + \frac{k\{w[(1-\cos wt) - k \sin wt] + (w-w_0)[k(1-\cos wt) + w \sin wt]\}}{\{k^2 + (w_0-w)^2\}(k^2 + w^2)} \right\} \right] \dots\dots\dots(20)$$

Nevertheless the expressions for the velocity components can be put as

$$V_x = \frac{a_y}{2} \left\{ \frac{\cos(w_0 t + p)}{\sqrt{k^2 + (w_0+w)^2}} + \frac{\cos(w_0 t - q)}{\sqrt{k^2 + (w_0-w)^2}} \right\} - \frac{a_x}{2} \left\{ \frac{\sin(w_0 t + p)}{\sqrt{k^2 + (w_0+w)^2}} - \frac{\sin(w_0 t - q)}{\sqrt{k^2 + (w_0-w)^2}} \right\} -$$

$$e^{-kt} \left\{ \frac{a_y}{2} \left\{ \frac{\cos(\omega t - p)}{\sqrt{k^2 + (\omega + \omega_0)^2}} + \frac{\cos(\omega t - q)}{\sqrt{k^2 + (\omega - \omega_0)^2}} \right\} + \frac{a_x}{2} \left\{ \frac{\sin(\omega t - p)}{\sqrt{k^2 + (\omega + \omega_0)^2}} - \frac{\sin(\omega t - q)}{\sqrt{k^2 + (\omega - \omega_0)^2}} \right\} \right\} \dots\dots\dots(21)$$

$$V_y = -\frac{a_x}{2} \left\{ \frac{\cos(\omega_0 t + p)}{\sqrt{k^2 + (\omega + \omega_0)^2}} + \frac{\cos(\omega_0 t - q)}{\sqrt{k^2 + (\omega - \omega_0)^2}} \right\} - \frac{a_y}{2} \left\{ \frac{\sin(\omega_0 t + p)}{\sqrt{k^2 + (\omega + \omega_0)^2}} - \frac{\sin(\omega_0 t - q)}{\sqrt{k^2 + (\omega - \omega_0)^2}} \right\} - e^{-kt} \left\{ \frac{a_x}{2} \left\{ \frac{\cos(\omega t - p)}{\sqrt{k^2 + (\omega + \omega_0)^2}} + \frac{\cos(\omega t - q)}{\sqrt{k^2 + (\omega - \omega_0)^2}} \right\} - \frac{a_y}{2} \left\{ \frac{\sin(\omega t - p)}{\sqrt{k^2 + (\omega + \omega_0)^2}} + \frac{\sin(\omega t - q)}{\sqrt{k^2 + (\omega - \omega_0)^2}} \right\} \right\} \dots\dots\dots(22)$$

Where $\tan p = k/(\omega + \omega_0)$ and $\tan q = k/(\omega - \omega_0)$

Or otherwise with $\tan \alpha = \frac{a_x}{a_y} \dots\dots(23)$

$$V_x = \frac{\sqrt{a_x^2 + a_y^2}}{2} \left\{ \frac{\cos(\omega_0 t + p + \alpha)}{\sqrt{k^2 + (\omega + \omega_0)^2}} + \frac{\cos(\omega_0 t - q - \alpha)}{\sqrt{k^2 + (\omega - \omega_0)^2}} \right\} - e^{-kt} \left\{ \frac{\cos(\omega t - p - \alpha)}{\sqrt{k^2 + (\omega + \omega_0)^2}} + \frac{\cos(\omega t - q - \alpha)}{\sqrt{k^2 + (\omega - \omega_0)^2}} \right\} \dots\dots\dots(24)$$

$$V_y = -\frac{\sqrt{a_x^2 + a_y^2}}{2} \left\{ \frac{\sin(\omega_0 t + p + \alpha)}{\sqrt{k^2 + (\omega + \omega_0)^2}} - \frac{\sin(\omega_0 t - q - \alpha)}{\sqrt{k^2 + (\omega - \omega_0)^2}} \right\} - e^{-kt} \left\{ \frac{\sin(\omega t - p - \alpha)}{\sqrt{k^2 + (\omega + \omega_0)^2}} + \frac{\sin(\omega t - q - \alpha)}{\sqrt{k^2 + (\omega - \omega_0)^2}} \right\} \dots\dots\dots(25)$$

Integrating (24) and (25) and employing the initial conditions (13), we can also find the position (x,y) of the electron at any time t.

But differentiating with respect to time t rather than {(17),(18)} or {(21),(22)} we can find the acceleration components in more simplified form:

$$f_x = \dot{V}_x = \frac{\sqrt{a_x^2 + a_y^2}}{2} \left[\omega_0 \left\{ \frac{\sin(\omega_0 t + p + \alpha)}{\sqrt{k^2 + (\omega + \omega_0)^2}} + \frac{\sin(\omega_0 t - q - \alpha)}{\sqrt{k^2 + (\omega - \omega_0)^2}} \right\} + e^{-kt} \left[\omega \left\{ \frac{\sin(\omega t - p - \alpha)}{\sqrt{k^2 + (\omega + \omega_0)^2}} + \frac{\sin(\omega t - q - \alpha)}{\sqrt{k^2 + (\omega - \omega_0)^2}} \right\} + k \left\{ \frac{\cos(\omega t - p - \alpha)}{\sqrt{k^2 + (\omega + \omega_0)^2}} + \frac{\cos(\omega t - q - \alpha)}{\sqrt{k^2 + (\omega - \omega_0)^2}} \right\} \right] \right] \dots\dots\dots(26)$$

$$f_y = \dot{V}_y = -\frac{\sqrt{a_x^2 + a_y^2}}{2} \left[\omega_0 \left\{ \frac{\cos(\omega_0 t + p + \alpha)}{\sqrt{k^2 + (\omega + \omega_0)^2}} - \frac{\cos(\omega_0 t - q - \alpha)}{\sqrt{k^2 + (\omega - \omega_0)^2}} \right\} - e^{-kt} \left[\omega \left\{ \frac{\cos(\omega t - p - \alpha)}{\sqrt{k^2 + (\omega + \omega_0)^2}} + \frac{\cos(\omega t - q - \alpha)}{\sqrt{k^2 + (\omega - \omega_0)^2}} \right\} - k \left\{ \frac{\sin(\omega t - p - \alpha)}{\sqrt{k^2 + (\omega + \omega_0)^2}} + \frac{\sin(\omega t - q - \alpha)}{\sqrt{k^2 + (\omega - \omega_0)^2}} \right\} \right] \right] \dots\dots\dots(26)$$

Squaring and adding (24) and (25) we have an expression for velocity

$$v^2 = \frac{a_x^2 + a_y^2}{4} \left[\left\{ \frac{1}{k^2 + (\omega_0 + \omega)^2} + \frac{1}{k^2 + (\omega_0 - \omega)^2} \right\} (1 + e^{-2kt}) + \frac{2\{\cos(2\omega_0 t + p - q) + e^{-2kt} \cos(p + q)\}}{\sqrt{k^2 + (\omega + \omega_0)^2} \sqrt{k^2 + (\omega - \omega_0)^2}} \right] - \frac{(a_x^2 + a_y^2)}{2} e^{-kt} \left[\left\{ \frac{\cos(\omega_0 t + p + \alpha)}{\sqrt{k^2 + (\omega + \omega_0)^2}} - \frac{\cos(\omega_0 t - q - \alpha)}{\sqrt{k^2 + (\omega - \omega_0)^2}} \right\} \left\{ \frac{\cos(\omega t - p - \alpha)}{\sqrt{k^2 + (\omega + \omega_0)^2}} + \frac{\cos(\omega t - q - \alpha)}{\sqrt{k^2 + (\omega - \omega_0)^2}} \right\} + \left\{ \frac{\sin(\omega_0 t + p + \alpha)}{\sqrt{k^2 + (\omega + \omega_0)^2}} - \frac{\sin(\omega_0 t - q - \alpha)}{\sqrt{k^2 + (\omega - \omega_0)^2}} \right\} \left\{ \frac{\sin(\omega t - p - \alpha)}{\sqrt{k^2 + (\omega + \omega_0)^2}} + \frac{\sin(\omega t - q - \alpha)}{\sqrt{k^2 + (\omega - \omega_0)^2}} \right\} \right] \dots\dots\dots(28)$$

Discussion and Conclusion:

After a lapse of time t, $e^{-kt} \rightarrow$

0 as $t \rightarrow \infty$ and so from (28), one gets, $v_1 =$

$$\frac{\sqrt{a_x^2 + a_y^2}}{2} \left\{ \frac{1}{\sqrt{k^2 + (w-w_0)^2}} - \frac{1}{\sqrt{k^2 + (w+w_0)^2}} \right\} \leq v \leq$$

$$\frac{\sqrt{a_x^2 + a_y^2}}{2} \left\{ \frac{1}{\sqrt{k^2 + (w+w_0)^2}} + \frac{1}{\sqrt{k^2 + (w-w_0)^2}} \right\} = v_2$$

.....(29)

Which, rectifies that as the time passes, the velocity of the electron attains the minimum and the maximum values v_1 and v_2 respectively as shown in (29).

Similarly, squaring and adding (26) and (27) we get its acceleration f:

$$f^2 = \frac{(a_x^2 + a_y^2)w_0^2}{4} \left[\left\{ \frac{1}{k^2 + (w_0 + w)^2} + \frac{1}{k^2 + (w_0 - w)^2} \right\} - \frac{2\{\cos(2w_0 t + p - q) + e^{-2kt} \cos(p + q)\}}{\sqrt{k^2 + (w+w_0)^2} \sqrt{k^2 + (w-w_0)^2}} \right] + e^{-kt} f_1 + e^{-2kt} f_2$$

Where f_1 and f_2 are not constants but circular functions of time t and are finite as $t \rightarrow \infty$. So as the time passes, $e^{-kt}, e^{-2kt} \rightarrow 0$, which confirms that in light of (29)

$$v_1 w_0 \leq f \leq v_2 w_0 \dots \dots \dots (31)$$

Equating equation (19) and (20) representing the position (x, y) of the electron at time t can be written as

After a significant time i.e. as $t \rightarrow \infty$, $e^{-2kt} \rightarrow 0$ so that (32) and (33) yields

$$x = \frac{\sqrt{a_x^2 + a_y^2}}{2 w_0} \left\{ \frac{\sin(w_0 t + p + \alpha)}{\sqrt{k^2 + (w+w_0)^2}} + \frac{\sin(w_0 t - q - \alpha)}{\sqrt{k^2 + (w-w_0)^2}} \right\} - \frac{a_x}{2 w_0} \left\{ \frac{(w+w_0)}{\sqrt{k^2 + (w+w_0)^2}} - \frac{(w-w_0)}{\sqrt{k^2 + (w-w_0)^2}} \right\} - \frac{e^{-kt}}{2} \{ f_1 a_x + f_2 a_y \} - \frac{a_y k}{2 w_0} \left\{ \frac{1}{\sqrt{k^2 + (w+w_0)^2}} - \frac{1}{\sqrt{k^2 + (w-w_0)^2}} \right\} \dots (32)$$

$$x = \frac{\sqrt{a_x^2 + a_y^2}}{2 w_0} \left\{ \frac{\cos(w_0 t + p + \alpha)}{\sqrt{k^2 + (w+w_0)^2}} - \frac{\cos(w_0 t - q - \alpha)}{\sqrt{k^2 + (w-w_0)^2}} \right\} - \frac{a_y}{2 w_0} \left\{ \frac{(w+w_0)}{\sqrt{k^2 + (w+w_0)^2}} - \frac{(w-w_0)}{\sqrt{k^2 + (w-w_0)^2}} \right\} - \frac{e^{-kt}}{2} \{ a_x k_1 (\cos wt, \sin wt) + a_y k_2 (\cos wt, \sin wt) \} + \frac{a_x k}{2 w_0} \left\{ \frac{1}{\sqrt{k^2 + (w+w_0)^2}} - \frac{1}{\sqrt{k^2 + (w-w_0)^2}} \right\} \dots (33)$$

$$R^2 = (x - x_1)^2 + (y - y_1)^2$$

$$= \frac{a_x^2 + a_y^2}{4 w_0^2} \left[\left\{ \frac{1}{k^2 + (w_0 + w)^2} + \frac{1}{k^2 + (w_0 - w)^2} \right\} + \frac{2 \cos(2w_0 t + p - q)}{\sqrt{k^2 + (w+w_0)^2} \sqrt{k^2 + (w-w_0)^2}} \right] \dots (34)$$

As t increases further i.e on the whole as

$t \rightarrow \infty$ because of $-1 \leq \cos(w_0 t + p - q) \leq 1$ get,

$$\frac{\sqrt{a_x^2+a_y^2}}{2 w_0} \left\{ \frac{1}{\sqrt{k^2+(w-w_0)^2}} - \frac{1}{\sqrt{k^2+(w+w_0)^2}} \right\} \leq R \leq \frac{\sqrt{a_x^2+a_y^2}}{2 w_0} \left\{ \frac{1}{\sqrt{k^2+(w+w_0)^2}} + \frac{1}{\sqrt{k^2+(w-w_0)^2}} \right\} \dots(35)$$

Where, R is the distance of electron from a fixed point P(x₁, y₁), given by

$$x_1 = -\frac{a_x}{2 w_0} \left\{ \frac{(w+w_0)}{\sqrt{k^2+(w+w_0)^2}} - \frac{(w-w_0)}{\sqrt{k^2+(w-w_0)^2}} \right\} - \frac{a_y k}{2 w_0} \left\{ \frac{1}{\sqrt{k^2+(w+w_0)^2}} - \frac{1}{\sqrt{k^2+(w-w_0)^2}} \right\}$$

$$y_1 = -\frac{a_y}{2 w_0} \left\{ \frac{(w+w_0)}{\sqrt{k^2+(w+w_0)^2}} - \frac{(w-w_0)}{\sqrt{k^2+(w-w_0)^2}} \right\} + \frac{a_x k}{2 w_0} \left\{ \frac{1}{\sqrt{k^2+(w+w_0)^2}} - \frac{1}{\sqrt{k^2+(w-w_0)^2}} \right\} \dots(36)$$

The above inequality suggests that as the time passes, the effect of damping partially dies away and the electron ultimately remains in motion with its distance R from the above fixed point fluctuating between two values r₁ and r₂ given by

$$r_1 = \frac{\sqrt{a_x^2+a_y^2}}{2 w_0} \left\{ \frac{1}{\sqrt{k^2+(w-w_0)^2}} - \frac{1}{\sqrt{k^2+(w+w_0)^2}} \right\}$$

$$r_2 = \frac{\sqrt{a_x^2+a_y^2}}{2 w_0} \left\{ \frac{1}{\sqrt{k^2+(w-w_0)^2}} + \frac{1}{\sqrt{k^2+(w+w_0)^2}} \right\} \dots(37)$$

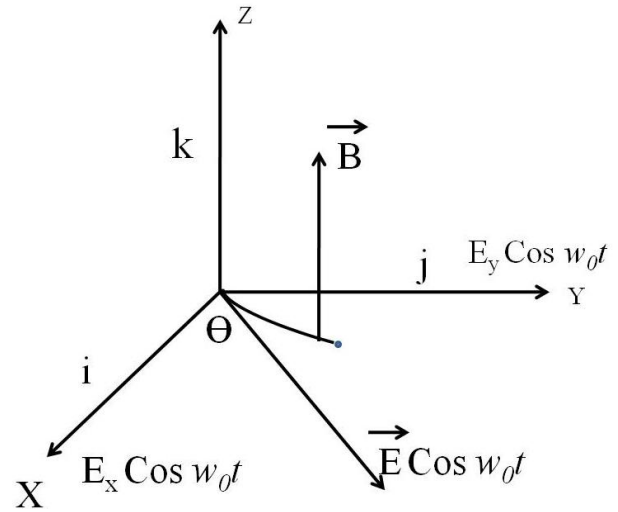


Figure 1, Path of an electron under mutually perpendicular alternative electric and constant magnetic fields.

References :

[1]Mahindra Singh Sodha, *Phenomenological theory of Electrical conduction, Bull IAPT, Vol 24, No 8, August 2007, PP. 240-245, 151.*

[2] S. N. Maitra, Damped motion of electron in electron in electric conductor due to presence of magnetic and alternative electric fields at right angles and closed form solutions, *Journal of Orissa Physical Society, Vol 16, No. 2, August 2009.*

Basics and Applications of Electrowetting on Dielectric (EW)

Dineshkumar Y. Turkar, Sandip M. Wadhai, Yogesh B. Sawane and Arun G. Banpurkar*

Department of Physics,
S P Pune University, Pune-411007
*e-mail: agb@physics.unipune.ac.in

(Submitted: 31-12-2014)

Abstract

The shape of liquid-droplet on planar surfaces is mainly governed by resultant surface tension forces at the vapour-liquid-solid boundary. In thermodynamic equilibrium, wetting of liquid or contact angle (CA) is given by Young-Dupr'e equation which is related to surface tensions of liquid, solid and interfacial tension of liquid-solid. The irreversible change in equilibrium wetting is possible by altering the surfaces and/or adding surfactant in the liquid. However, controlled and reversible wetting is desired in several applications like liquid-lens, ink-jet printing, droplet transport through micro-fluidic chip etc. Currently this is achieved by incident light, electric field, thermal gradient, magnetic field etc. The electric field induced wetting commonly termed as Electrowetting on dielectric (EWOD or EW) is the most successful method allowing fast and reversible change in wetting of aqueous and non aqueous droplet on dielectric surfaces. EW is currently implemented in variety of applications such as video displays, adaptive lens systems in cell-phone cameras, smart window panels etc. In the present review, we discuss basic EW phenomenon and governing equations. The experimental results related to EW based liquid lens system are discussed. The upcoming technology and challenges of EW are discussed at the end.

Introduction:

The dew on a grass leaves and spider web appears as if pearl necklaces fascinating the mankind since long time. The water bead on “Lotus” leaf has been a symbol of eternal purity from all the odds... *“One who does all work as an offering to the Lord, abandoning attachment to the results, is as untouched by sin [or Karmic reaction] as a lotus leaf is untouched by water (Bhaqaved Gita).* New born baby starts her effortless breath due to presence of surfactant in the alveoli. Trouble free washing of utensil and cloths take place in presence of magic liquid called detergent, oil recovery from reservoir requires additives in the water....there is endless list of applications that requires basic understanding of wetting property of liquid on solid surfaces and their control.

Thomas Young in 1805 has described the equilibrium wetting of liquid droplet on plane surface in terms of contact angle made by the liquid on solid surface¹. This mathematical equation is based on the force balance at the air-liquid-solid interface called as three-phase contact line (TCL). Figure 1 illustrates this force balance at TCL.

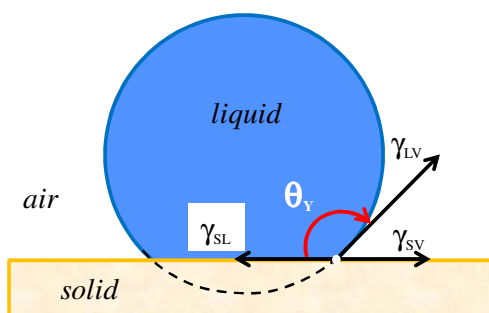


Fig. 1: The contact angle θ_Y on a planar surface is due to surface tension force balanced at every point of TCL

Young-Dupr’e equation relating surface tensions to the contact angle is given as

$$\cos\theta_Y = \frac{\gamma_{SV} - \gamma_{SL}}{\gamma_{LV}} \dots\dots\dots(1)$$

Where θ_Y is Young’s contact angle and surface tension forces described as γ_{SL} – solid-liquid, γ_{SV} –solid-vapour and γ_{LV} – liquid-vapour. This clearly shows that the contact angle of liquid is mainly related to surface tensions.

Many times surface-tension force can also be viewed as surface energy per unit area therefore above Young’s condition could be obtained by minimizing surface-energy for constant droplet volume. Thus free liquid volume forms spherical shape to minimize surface energy. The gravitational force also influences the shape of liquid volume. The interplay of the gravity and surface tension forces allows the liquid to form a bead or puddle. This is decided by the parameter called capillary length, $\kappa^{-1} = \sqrt{\gamma/\rho g}$ where ρg is gravitational force per unit volume and γ is liquid surface energy per unit area. For instance capillary length for water is 2.73 mm, hence water droplet below 2.7 mm size favour spherical shape while above this size, it forms a puddle.

Many planar surfaces like polymer sheets, metals and metal-oxides coated surfaces exhibits varied contact angle for water. On the basis of water

contact angle (θ_Y) surfaces are characterized as hydrophilic surface ($0^\circ < \theta_Y < 90^\circ$), hydrophobic surface ($90^\circ \leq \theta_Y < 150^\circ$) and superhydrophobic surface ($150^\circ \leq \theta_Y < 180^\circ$). Thus Lotus leaf and many plant surfaces exhibit superhydrophobic state. And complete spreading of water on clean glass shows hydrophilic state of glass.

In addition to the naïve definitions of the wetting, Zisman showed that the wettability of a liquid on surfaces is not only decided by the surface energy of solids or liquids but it depends on the polarizabilities². Zisman's rule says that 'A liquid spreads completely if it is less polarizable than the solid' which in general explains why liquid Helium with its low polarizability spreads on most solid. Also spreading of oil on water surface is due high polarizability of water than oils. Therefore changing polarizability at liquid-solid interface is necessary for alteration in wetting.

Several conventional techniques are currently used to bring changes in wetting on solid surfaces. For instance, thermal gradient at interface changes surface tensions of both liquid and solids is termed as thermo-capillarity³. In the photowetting, the light on solid-liquid interface is made incident to alter the surface tensions hence changes CA⁴. In case of magneto-wetting, external magnetic field is used to induce the wetting. Also external electric field is used to alter this wetting is known as electrowetting⁵. Out of these above schemes Electrowetting has gain tremendous impetus due to several advantages in design and simplicity of the process. This is also commonly called as electrowetting on dielectric (EWOD) or electrowetting (EW). This technique is very successful in changing surface-energy or contact angle of liquid on dielectric surface by several degrees ($\Delta\theta \sim 70$ to 90°) with the application of electric voltage across the droplet and the control electrode buried in the dielectric.

Figure 2 shows generic EW setup used to change the wetting of conductive liquid on dielectric surface.

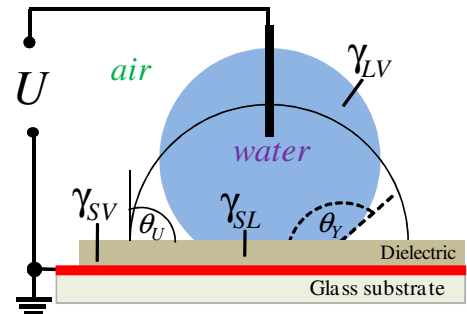


Fig. 2: Schematic shows basic EW setup the conductive electrode buried in the dielectric is shown in red colour.

Here U is an external voltage either low frequency alternating current (AC) or direct current (DC). The Young's contact angle is denoted by θ_Y at $U = 0$ V and reduction in CA for external voltage U is shown by $\theta(U)$. Another wire free geometry is most common wherein electric field is applied between electrodes buried in the dielectric as shown in Fig 3 and liquid droplet is free from any direct electrical contacts.

In both these cases electrical charge density or polarization at the liquid-solid interfaces is altered by the external applied voltage. Thus evolution of electrostatic energy at solid-liquid interface due to electric charge density alters surface-energy balance at solid-liquid interface changing the wetting of liquid as function of external voltage. The electrostatic energy due to charge density reduces to zero upon removal of the external voltage restoring normal wetting state of the liquid. Therefore, EW process is fast and can be realized on the time scale of the droplet hydrodynamic relaxation time scales, which depends on viscosity, surface-tension and droplet size.

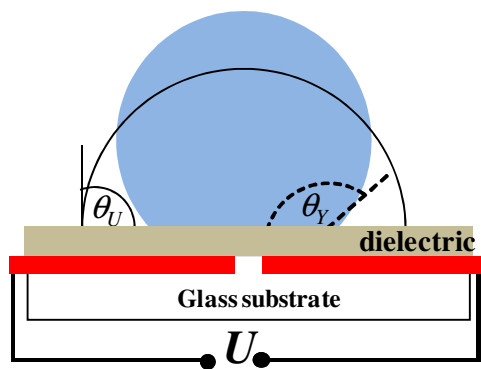


Fig. 3: Schematic shows wire-free EW setup and conductive electrodes (red) are buried in the dielectric.

The present form of the generic and wire-free electrowetting setups has been derived from the ingenious work on electro-capillarity by French Scientist Gabriel Lippmann's (1875)⁶. Lippmann showed that the height of the mercury in contact with diluted electrolyte in fine capillary tube is function of the voltage across the interface. An insulating double layer is often formed at two dissimilar electrolytes liquid interface analogous to the contact potential at metal-semiconductor junction. The electrical double-layer (EDL) at mercury-electrolyte interface is mainly due to the separations of ions at the interfaces. The EDL is feeble and break-down at moderate external voltage. Thus desired wetting is not possible on liquid-liquid interfaces. Lippmann electro-capillarity experiment was not attracted in past several years. After 1990 this phenomenon is revisited in new form. A thick dielectric layer is introduced at liquid-solid interface. A voltage is then applied between liquid and rigid planar electrode. Here dielectric layer avoids direct liquid contact with electrodes⁷. This is generic electrowetting geometry commonly known as electrowetting on dielectric (EWOD) or electrowetting (EW) which finds numerous

application includes variable focal lenses⁸, video speed display⁹, laser mirrors and beam splitters¹⁰, tensiometer¹¹, rheometers¹² and many digital (droplet) microfluidic devices for micro-fluidics and lab-on-chip devices¹³.

In the present review, we used water drop of size about 1.5 mm which is blow capillary length hence surface tension dominates gravity force. Thus 1.5 mm size water droplet assumes near perfect spherical cap shape. At constant volume of droplet, the other geometrical parameters of spherical cap like base radius, radius of curvature etc. can be related to contact angle θ . Electrowetting is used to bring changes in contact angle θ using external voltage thus all geometrical parameters of spherical cap can be function of applied voltage.

After this brief introduction, we presented theoretical model for EW on spherical cap using Lippmann's approach. Subsequently energy minimization approach is presented to derive the same EW equation. The close form equations relating geometrical parameters of spherical cap as a function of contact angle is discussed. Basic experimental procedure for studying the EW is discussed in detail. Finally we present results and discussion on EW spherical cap as tunable liquid lens.

Electrowetting on Dielectric: EW equation shows variation in contact angle as function of voltage magnitude. This is derived by Lippmann for the first time using thermodynamics and electro-chemical approach. In the following we present Lippmann's original approach and subsequently same relation is derived using energy minimization principle. Several other approaches for deriving EW equation can be found in review by J.C. Baret and F. Mugele⁵

(i) Thermodynamic and Electrochemical approach for EW equation:

Figure 4 shows generic EW setup with and without external voltage between conductive drop and bottom electrode. The presence of charges at interface due to external voltage between two conducting medium affects the surface tension of liquid drop in contact with dielectric, this is typically called as electrocapillarity⁶. Electric potential at the interface produces surface-charge density at the interface. We neglect the fringing field at the droplet boundary and try to setup an equation of the thermodynamic energy change.

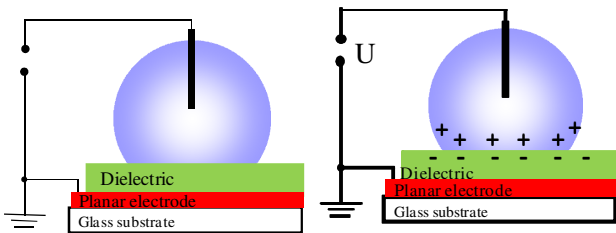


Fig. 4 Schematic shows generic setup and change density at the liquid-solid interface.

At equilibrium temperature T and pressure P , The thermodynamic potential (Gibbs free energy) is given by¹⁴

$$dG = \gamma dA - edU \dots\dots\dots(2)$$

Where γ is surface tension and e is electronic charge at interface. dG is change in thermodynamic free energy for external voltage dU . Here γdA is the work done in reversible change dA in area A of the surface of separation.

Thermodynamic potential is replaced by its surface part only at constant pressure and temperature.

$$dG_s = \gamma_{SL} dA - edU \dots\dots\dots(3)$$

At constant potential U , $dU = 0$ and above eq. becomes

$$G_s = \gamma_{SL} A \dots\dots\dots(4)$$

Upon applying voltage dU an electric charge density builds up spontaneously at solid-liquid interface consisting of charge on metal surface other oppositely charged ions on liquid side interface. It results in reduction of surface tension as:

$$d\gamma_{eff} = -\sigma_{SL} dU \dots\dots\dots(5)$$

Where, σ_{sl} is surface charge density at solid-liquid interface. Total effective surface tension between solid liquid is obtained by integrating above Eq. 5

$$\gamma_{SL}^{eff} = \gamma_{SL} - \int_0^U \sigma_{SL} dU \dots\dots\dots(6)$$

$$\gamma_{SL}^{eff} = \gamma_{SL} - \frac{C^* U^2}{2} \dots\dots\dots(7)$$

Where capacitance per unit area, $C^* = \frac{\epsilon\epsilon_0}{d}$ with $\epsilon\epsilon_0$ is permittivity and d is the thickness of the dielectric medium.

Young equation gives the equilibrium contact angle of liquid drop on solid surface is given by eq.1. Substituting the value of effective interfacial tension (Eq. 1) of solid in contact with liquid and in the presence of external voltage in Eq. 7, which reads as:

$$\cos\theta(U) = \cos\theta + \frac{C^* U^2}{2\gamma_{LV}} \text{ or}$$

$$\cos\theta(U) = \cos\theta + \frac{\epsilon\epsilon_0 U^2}{2d\gamma_{LV}} \dots\dots\dots(8)$$

$$\cos\theta(U) = \cos\theta + \eta \dots\dots\dots(9)$$

where $\eta = \frac{\epsilon\epsilon_0 U^2}{2d\gamma_{LV}}$ is the dimensionless

electrowetting number indicates relative strength of electrical surface energy to interfacial surface energy. Equation 8 or 9 is termed as Young-Lippmann equation relating the change in contact angle with applied voltage U . This equation is valid for direct current (DC) and alternating

current (AC) voltages. In case of the AC voltage root mean square (r.m.s.) values are considered as voltage amplitude. The above equation is also derived using energy minimization.

(ii) EW Equation from Energy Minimization Approach¹⁵:

In this model total work done in setting charge density at liquid-solid interface and charge density withdrawn from the battery is considered. The energy from the battery is utilized to charge the liquid-solid interface and counter charge on the planar bottom electrodes as shown in Fig 5. The thermodynamics system is droplet, dielectric layer, metal electrode, and the voltage source (Battery). Throughout the derivation, we assume that the system is in equilibrium at constant potential U and at constant temperature T .

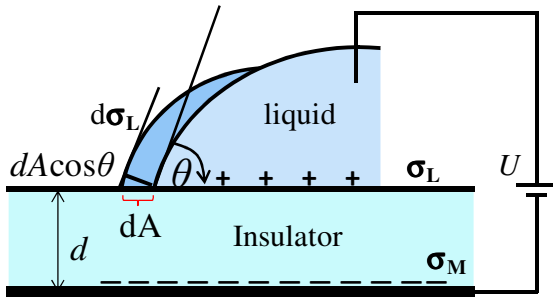


Fig. 5: A conductive droplet sitting on a dielectric surface. A battery perform work in setting a charge density at liqid-solid interface and countercharge density at bottom conductive electrode.

We focus on the change in free energy due to an infinitesimal increase in base area dA of the droplet on the solid surface surrounded by vapor. When a potential U is applied, a charge density σ_L is builds up in liquid phase and induces an image charge density σ_M on the metal electrode. An infinitesimal increase of the base area dA results in a contribution to the free energy from the surface energies also an energy contribution to the additional charge density $d\sigma_L$ liquid and its

image charge density $d\sigma_M$ on the metal electrode. The voltage source performs work dW_B .

The free energy change (dF) of the system can be written as:

$$dF = \gamma_{SL}dA - \gamma_{SV}dA + \gamma_{LV}dA \cos \theta + dE_{el} - dW_B$$

.....(10)

where dE_{el} is energy stored in the electric field between the liquid and the counter electrode and dW_B is work done by the battery.

In the absence of external field $dE_{el} = dW_B = 0$

and on minimizing with respect to area $\frac{dF}{dA} = 0$

this gives Young Eq. (1)

For a non- zero potential, we need to include the energy of the charge distribution. We know that, the electrostatic energy per unit area below liquid is

$$\frac{E_{el}}{A} = \int_0^d \frac{1}{2} \vec{E} \cdot \vec{D} dz, \text{ where } z \text{ is the coordinate perpendicular to the surface, } d \text{ the thickness of the insulating layer, } \vec{E} \text{ the electric field, and } \vec{D} \text{ the charge displacement, with } \vec{D} = \epsilon \epsilon_0 \vec{E}.$$

The increase of free energy due to the charge distribution in the liquid, upon an infinitesimal increase of droplet base can be written as.

$$\frac{dE_{el}}{dA} = \frac{U\sigma_L}{2}.$$

Where σ_L is the charge density at liquid-solid interface and U is electric voltage.

The battery performs the work to redistribute the charges at interface as well as on the bottom electrode. Therefore the work done by the battery per unit area is given by $\frac{dW_B}{dA} = U\sigma_L$.

Substituting these values in Eq. 10, we get

$$\frac{dF}{dA} = \gamma_{SL} - \gamma_{SV} + \gamma_{LV} \cos \theta + \frac{1}{2}U\sigma_L - U\sigma_L$$

At equilibrium, $\frac{dF}{dA} = 0$, above equation becomes

$$\gamma_{LV} \cos\theta(U) = \gamma_{SV} - \gamma_{SL} + \frac{1}{2} U \sigma_L \quad \text{which gives}$$

$$\cos\theta(U) = \cos\theta + \frac{1}{2} \frac{U \sigma_L}{\gamma_{LV}}$$

now the charge density can be written as

$$\sigma_L = E \epsilon \epsilon_0 = \frac{U \epsilon \epsilon_0}{d} \text{ where } E = U/d \text{ is the electric}$$

field. Then above equation becomes

$$\cos\theta(U) = \cos\theta + \frac{1}{2} \frac{\epsilon \epsilon_0 U^2}{d \gamma_{LV}} = \cos\theta + \eta \dots\dots\dots(11)$$

This is the same as Young’s-Lippmann equation. The equation indicates that contact angle for a given voltage varies directly as permittivity of the dielectric medium and inversely with interfacial tension of the liquid. Thus a droplet of low interfacial tension on insulator of high dielectric constant is preferred in the EW. Equation 11 clearly indicates that with increasing voltage magnitude, the contact angle decreases and opposite is not possible. Thus high contact angle at zero voltage is desired for large tuning range. For instance, if the EW is performed on water droplet then low energy dielectric surface made from fluoropolymer with high dielectric breakdown field is preferred.

In most of the circumstances, oil ambient is used to reduce interfacial tension. Further it arrests the evaporation of aqueous droplet and provides thin lubricating film between droplet and substrate.

In the next section we present geometrical formalism for spherical cap of liquid drop.

Spherical Cap

A tiny liquid droplet sitting on the planar surface forms a spherical cap. It is a part of sphere as shown in Figure 6.

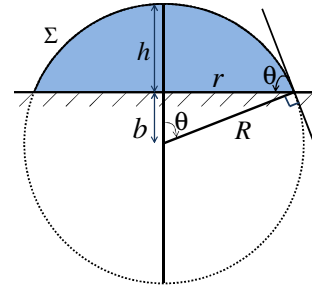


Fig. 6: A tiny water droplet of volume ~ 10 µl sitting on a planar surface is approximated as spherical-cap. For a constant volume droplet, h is droplet height, R is radius of curvature, θ is contact angle, r is base radius and Σ is surface area exposed to the ambient.

This approximation is valid for droplet diameter or length is below a length scale called as capillary length $\kappa^{-1} = \sqrt{\gamma/\rho g}$ where, γ is surface tension, ρ is the liquid density and g is acceleration due to gravity. For water λ = 2.7 mm. The elementary mathematics is used to derive relations between the contact angle θ and geometrical parameters like drop contact area r, radius of curvature R, exposed surface area Σ and drop height, Here volume (V_{cap}) of a droplet is kept fixed.

$$R = \left[\frac{3V_{cap}}{\pi(2 - 3 \cos \theta + \cos^3 \theta)} \right]^{1/3} \dots\dots\dots(12)$$

$$r = R \sin \theta = \left[\frac{3V_{cap}}{\pi(2 - 3 \cos \theta + \cos^3 \theta)} \right]^{1/3} \sin \theta \dots\dots\dots(13)$$

$$h = R (1 - \cos \theta) \dots\dots\dots(14)$$

$$\Sigma = 2\pi R h \dots\dots\dots(15)$$

The base area in contact with solid surface also given as $A_{base} = \pi r^2$. The drop of known volume on solid substrate can be deposited using micropipette. The volume is input parameter in this equation. Indeed the above common parameters are function of contact angle θ. In case

of the electrowetting this θ is function of the external voltage. Thus the above parameters of the spherical cap become function of the external voltage.

Experimental Techniques:

(i) Dielectric Coating for EW Application:

The materials for dielectric layer and bottom electrodes are not very specific in the EW applications. Any metallic surface covered with suitable hydrophobic film can be used to study EW phenomenon. Most of the EW studies were done on Teflon (PTFE) film. It has low surface energy hence large CA of water. The commercially available films are in the range of tens of micrometer therefore high voltage is required to get the desired contact angle change. In several EW study at moderate voltages (< 100 V), thin coating from Teflon AF (DuPont USA)¹⁶ or Cytop (Asahi Glass, Japan)¹⁷ solution are commonly used. The coating from both these solution provides thickness in the range of nanometer to micro-meter that depends mainly on the process parameters. Usually dip-coating and spin coating is used for this purpose. Brief procedure for Teflon AF dip-coating is described below. The Teflon AF dielectric layer can be dip-coated on any conductive surfaces. Here we used commercial Indium Tin Oxide (ITO) glass as an electrode. At the beginning, ITO glass was thoroughly cleaned successively in ultrasonic bath of diluted soap water, Acetone, isopropanol and ethanol. Finally it was dried in dry nitrogen jet. A dip coating machine is used for this dielectric coating. We used solution of amorphous fluoropolymer Teflon AF1600 (DuPont, USA) in perfluorinated solvent FC40 (3M) at 6% w/v concentration. The ITO glass was slowly dipped at the speed of 15 cm/min and withdrawn after 10

sec. at same speed. These films were pre-dried in laminar flow and then in oven at 110 °C for 30 min. These films were cooled to room temperature and one more Teflon AF layer was applied using same experimental parameters. Finally substrates were heated at 160 °C for 10 minutes and 240 °C for 30 minutes in a vacuum oven for complete removal of solvent. The EW experiment also can be performed on several dielectric surfaces such as polystyrene¹⁸, PVDF, SU8, PMMA, Parylene and multilayers of SiO_x-SiN_x, Al₂O₃¹⁰ and Ti₂O₅¹⁹ covered with thin hydrophobic layer of either Teflon or Cytop etc.

Experiment Arrangement for Electrowetting:

The Electrowetting phenomenon can be conveniently studied using direct current (DC) as well as alternating current (AC) voltages. Electrowetting with DC voltages, one requires a variable DC power supply with the stable voltage magnitude from 0 to 200 V. The maximum voltage range can be decided from the dielectric thickness values. This voltage rating is sufficient for the dielectric layer of thickness 2-3 μm . For thick dielectric film like commercial Teflon tape, one needs a power supply rating of about 1 kV. These power ratings are same for AC voltage source. In case of AC voltage the frequency should be above 500 Hz and below 10 kHz. The lower cutoff frequency is limited by hydrodynamic response time, $\tau = l \frac{\mu}{\gamma}$, where l , is droplet diameter and μ is the liquid viscosity. The droplet diameter is mainly limited by the capillary length. The higher cut-off frequency is mainly decided by the droplet conductivity. At sufficient higher frequency, dielectrophoretic effects prevails therefore, EW which is derived from conductive droplet model, fails to predict the

change in CA with applied voltage magnitude at high frequency AC voltages.

Typical setups we used to prove the results are discussed here. A schematic of the experimental setup is shown in Fig. 7. It consists of a rectangular cuvette for placing a conductive substrate. A Function generator (HP 33120 A) was used as AC voltage source. Then this signal was amplified using a custom built high voltage amplifier (Kemtec Engineering, Pune). The amplified voltage was given to a water drop with the bottom electrode at ground potential.

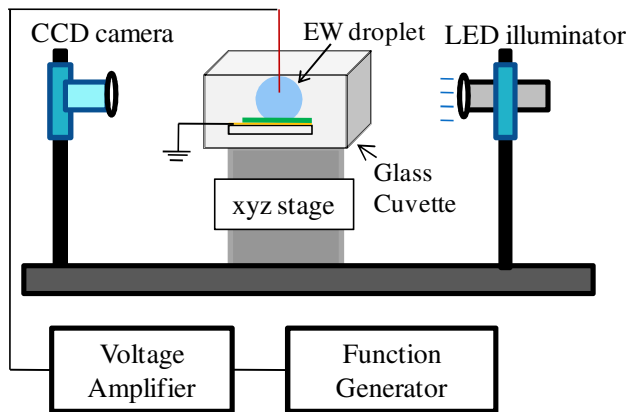


Fig. 7: Schematic of the experimental set up used for studying electrowetting on dielectric in oil ambient.

A CCD camera attached with the low magnification microscope was used for imaging the contact angle of the droplet at specified applied voltages. This drop was back illuminated using an LED torch. All these were axially aligned and fixed on the stand as shown in the figure. During the experiment, the cuvette table was kept horizontally flat using xyz position screws. The cuvette was filled with silicone oil. The level of the silicone oil was adjusted to keep the water drop submerged. A small amount of salt (1 mg /10 ml) was added in water to increase the conductivity. The salt does not change the surface tension of water but increases the conductivity. Using a micro pipette, a water drop

of 8 μl was dispensed on a thin dielectric film. This is a sessile drop arrangement as shown in Fig. 7. After the nice optical arrangement, AC power supply was switched on and a drop image was seen on the computer screen. First contact angle was measured at 0 V. Then voltage was increased in steps of 4 V. For each AC voltage, the corresponding droplet image was saved in the computer. The experiment was repeated many times and for increasing and decreasing voltage cycles. We used 1 kHz AC frequency in this study. The droplet image was analyzed using open source ImageJ 1.48 image processing software.

The results of the EW are discussed in the following section.

Result and Discussion:

We have studied the electrowetting on dielectric by using wired geometry and interdigitated wire-free geometry, and the response curves have been verified by plotting the Young-Lippmann relation. Figure 8 shows the snapshot of EW water droplet in silicone oil ambient and on a wired electrowetting setup. It clearly shows a decrease in CA with increasing voltages.

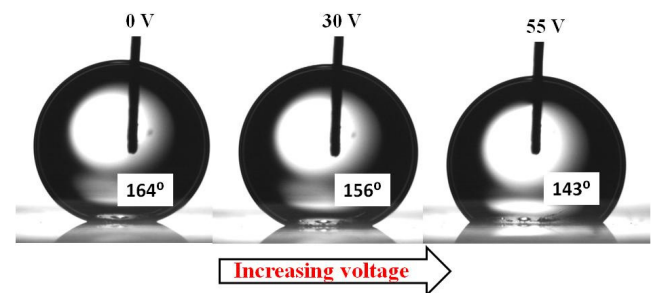


Fig. 8: Snapshots of EW on a water droplet using a wired setup for increasing voltage magnitude.

Also, we have investigated electrowetting behavior for wire-free geometry on interdigitated electrodes. Figure 9 shows the snapshot of droplets illustrating contact angle variation with increasing

voltage for wire free geometry. Nature of response curves for wire free electrowetting geometry has close resemblance with wired geometry.

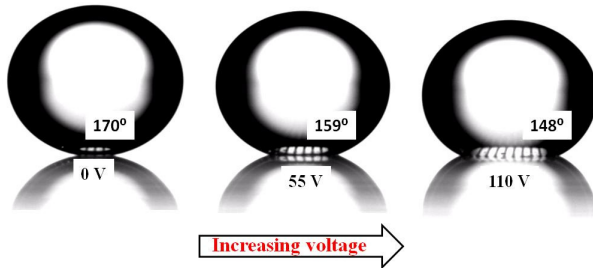


Fig. 9: Snapshot of electrowetted droplets with increasing voltage for wire free geometry.

The plot of the contact angle against applied voltage is shown in Fig. 10.

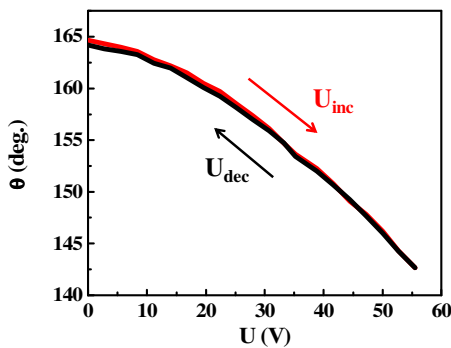


Fig. 10: Contact angle change with applied voltage for increasing and decreasing magnitude.

We then verify the electrowetting nature by plotting Young-Lippmann relation. The plot shown in Fig. 11 depicts cosine of the change in contact angle against voltage square. Indeed this shows linear variation. The change in contact angle with voltage shows excellent recovery. When voltage decreases to zero, the contact angle also attains the initial value.

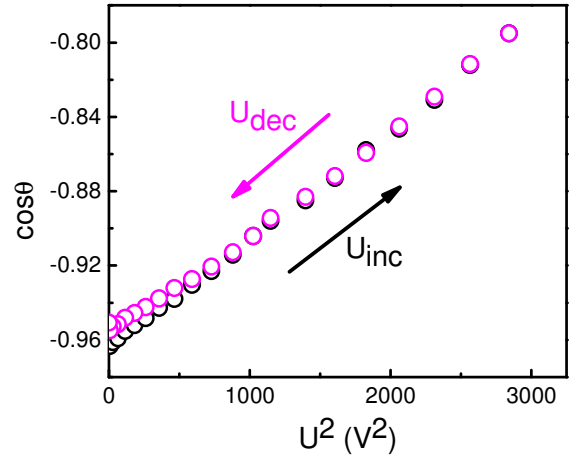


Fig. 11: Electrowetting on water drop: a contact angle change $\cos \theta(U)$ against voltage square U^2 is plotted for $U = 0 \text{ V}$ to $U_{\max} = 53.3 \text{ V}$ (rms). The increasing and decreasing voltage level are depicted as U_{inc} and U_{dec} respectively.

This plot can be used to obtain several physical parameters like interfacial tension of water-oil, dielectric constant and the thickness. From Young-Lippmann equation the slope of $\cos \theta(U)$ versus U^2 curve has the value $\frac{\epsilon \epsilon_0}{2d \gamma_{LV}}$ where $\epsilon \epsilon_0$ is

the permittivity of the dielectric medium, d is thickness and γ_{LV} is the interfacial tension of water with respect to the surrounding medium.

We measured thickness of Teflon film using profilometer and found to be $3.66 \mu\text{m}$. The dielectric has to be as thin as possible but thin dielectric ($\sim \text{nm}$) often shows dielectric breakdown before achieving a desired change in contact angle. These values can be followed using EW slope value of the plot shown in Fig. 11. The slope of the graph between $\cos \theta(U)$ and U^2 is found to be 5.671×10^{-5} SI unit. From the slope capacitance per unit area (C^*) is calculated which is $4.514 \mu\text{Fm}^{-2}$ which is constant for the given configuration of the dielectric medium. Contact angle hysteresis of around 3° can be seen during

reverse cycle. This is advantage of silicone oil ambient to the water droplet.

This plot can be employed to obtain a desired unknown value from constants. Recently such EW results are used for the estimation of interfacial tension of unknown liquids. We also determine the interfacial tension of water-silicone oil which is found to be 38 mNm^{-1} in excellent agreement with the reported value¹¹. We now use the results of Electrowetting and the spherical cap model to demonstrate the variation in droplet geometry as a function of applied voltage.

Figure 12 shows plot of variation in base area of the droplet as a function of square of voltage.

Here we use the droplet images and estimated the base radius to find out the base area. Here it is called as experimentally determined base area (S_{exp}). The plot shows that base area linearly varies with square of applied voltage U .

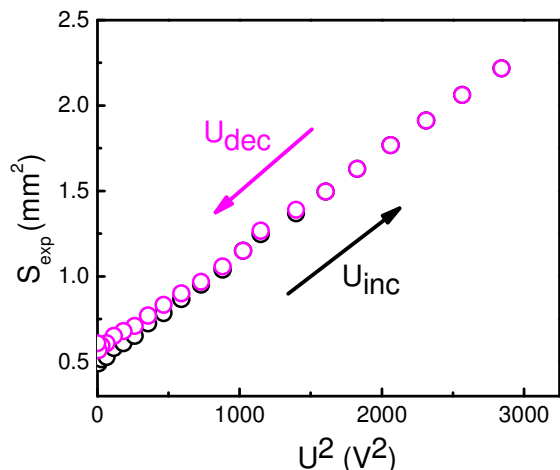


Fig. 12: The base area of the droplet determined experimentally is plotted against voltage square.

We also calculated the base area of the droplet from base radius related to contact angle as given in the Eq. 13. The EW contact angles corresponding to all the voltage values are used to determine the value of the base area. This base area is termed as theoretical base area S_{the} plotted as voltage square in Fig. 13.

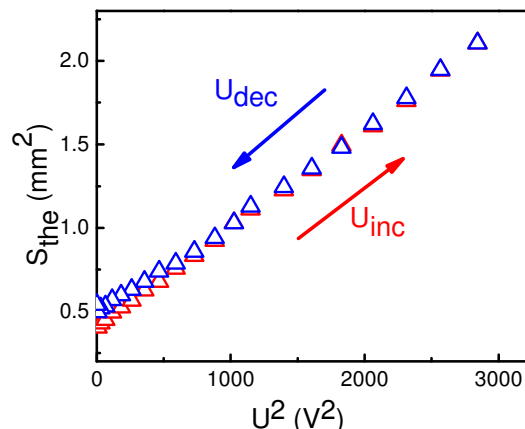


Fig. 13: Plot shows a base area of droplet calculated from closed form of spherical cap plotted against U^2 . The graph is again linear with voltage square.

Here the plot shows linear variation with voltage square. We compare our experimental results with the value estimated from spherical cap model in Fig. 14.

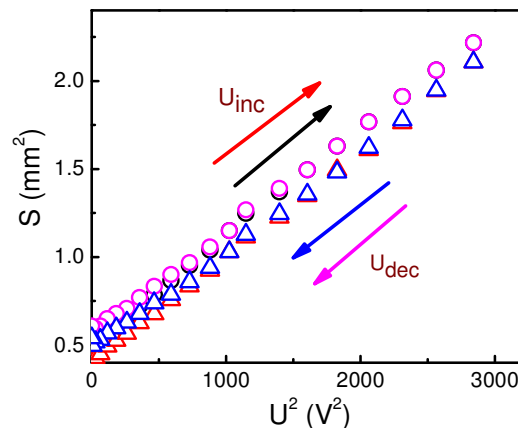


Fig. 14: Comparison between experimentally determined base area and theoretically calculated base area for given variation in potential. Both are closely overlapping with each other.

Experimentally measured and theoretically calculated base area both are matching fairly well. This linear nature helps in tuning of base area of the droplet with respect to applied voltage. In the working regime of contact angle θ , varying from 164° to 143° , is almost linear with U^2 . The small

deviation in the experimental and theoretical value is mainly due to the error in volume measured by the optical techniques and actual volume of the droplet taken from micro-pipette.

Figure 15 shows variation in capacitance of the system as a function of applied voltage square

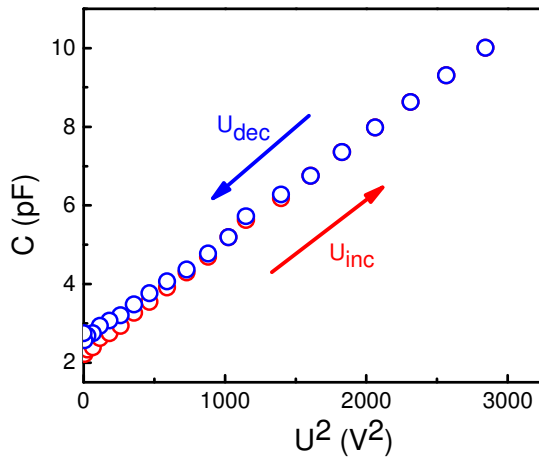


Fig. 15: The capacitance of the system plotted against square of applied voltage.

The capacitance of the system shows fairly linear variation with the voltage square. In EW based technique capacitance of the system is varied by external voltage and not by any mechanical movement. This is implemented in several electronic- frequency tuning devices.

The liquid droplet forming a nice spherical cap is known for its optical properties like lens. A droplet sitting on leaves acts as lens. EW provides continuous change in contact angle with external voltage. The leasing property of such droplet depends on the radius of curvature. Therefore we plot radius of curvature of EW droplet as a function of voltage square as show in Fig. 16.

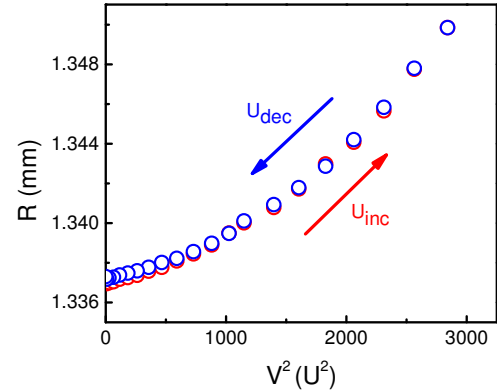


Fig. 16: Plot of Radius of curvature R versus voltage square.

The dependency of R on contact angle θ , and hence on U is quite complex. Dependency can be seen from Eq .12 However, voltage dependent changes in the radius of curvature are possible through EW. This does not require any mechanical input.

The droplet height variation can be used for EW based actuation. Figure 17 shows variation in the droplet height as a function of voltage square.

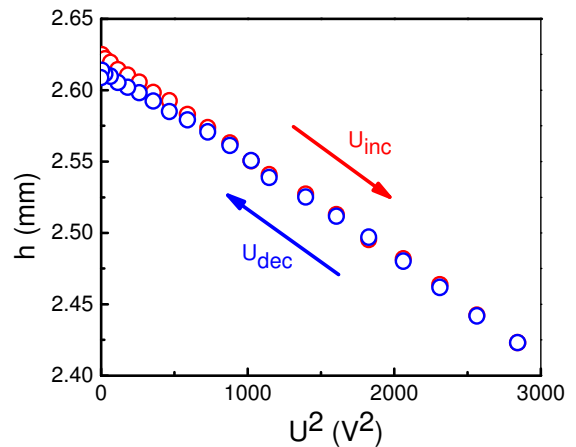


Fig. 17: Behavior of height of the drop on voltage square.

This shows that droplet height h decreases linearly with voltage square. Typically the mechanical

actuation in micrometer range can be easily achieved using EW.

The surface area in contact with ambient (here silicone oil) is estimated from Eq. 15 and plotted in Fig. 18.

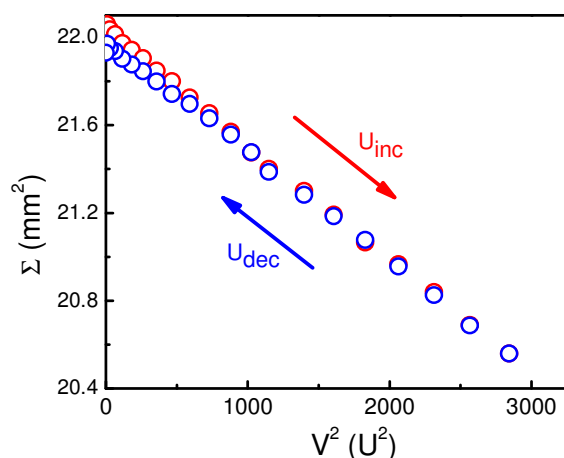


Fig. 18: Surface area of spherical droplet in contact to Silicone oil is plotted against voltage square.

The plot shows linear variation in the surface area with the voltage square.

We demonstrated that various geometrical parameter of electrowetted spherical cap can be varied by external voltage. This is non-contact method also reversible and high reproducibility. The oil ambient arrest evaporations thus it has high self-life. More applications of EW are discussed in the tutorial review by Shamai *et al*²⁰.

In the development of commercial applications especially the liquid lens, Bruno Berge⁸ has developed for the first time and set up a production unit named “Varioptics” in Lyon, France²¹. During the same time EW has been used for video speed display. A Dutch company “Liquivista” founded in 2006 at Eindhoven as a spin-off from Philips has developed colour e-paper video screens that can work in the presence and absence of backlight²². More recently, Mishra *et al* demonstrated ideal aspherical lens by applying electric field to a drop entrapped in an aperture

controlled hydrostatically²³. Herein, liquid-liquid meniscus shape is altered by simultaneously altering the electrostatic force and Laplace pressure. In this lens system, along with alteration of focal length, longitudinal spherical aberration (LSA) value can be altered achieving enhanced optical performance.

The EW based high speed actuation of micro-lens array has been recently demonstrated. The focal length of all 100 micro-lens array has been simultaneously modulated at frequency beyond 1 kHz²⁴. In case of the micro-fluidics lab-on-chip systems, electrowetting principle is used to create electrostatic potential well for the droplet sorting and manipulation of droplet in a desired micro-channel²⁵. The EW principle is also used in the fundamental studies that involve controlled wetting transition from superhydrophobic Cassie-Baxter state to Wenzel state on pillar-structured surface²⁶. Recently a wire-free electrowetting also called as dielectrowetting is used for the high resolution and high speed optical shutters which can be used as large area optical shutters in household window applications²⁷.

Many new application based on the EW as well as dielectrowetting principle can be envisaged in the future. However, there are some limitations in EW phenomenon²⁸. The basic limitation is as follows: Theoretically, Young-Lippmann equation states that CA decreases to any amount (complete wetting) with external applied voltage. In practical situation, one can decrease CA to a certain level well above the complete wetting state and reaches to saturation state. Figure 18 shows the CA saturation behavior in the EW. In the saturation regime, applied voltage does not cause any change in CA deviating from Young-Lippmann eq.

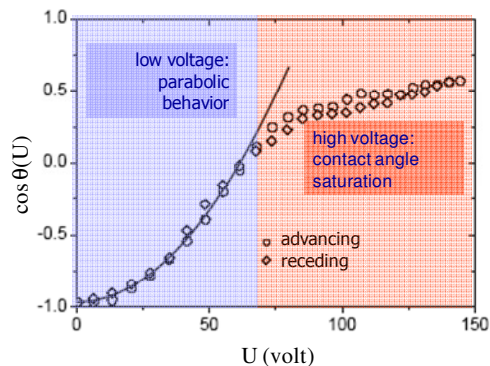


Fig. 18: CA variation $\cos \theta (U)$ plotted as applied voltage U .

Several theories are proposed to explain the CA saturation such as ionization of air at three phase contact line, charge trapping, dielectric leakage²⁹⁻³¹, defect in dielectric and dielectric breakdown. However consensus amongst the theories has not been reached yet. Therefore EW and dielectrowetting principle is being continuously used in the Young-Lippmann regime for increasing number of applications discussed in this article.

Conclusions:

In conclusion, we presented a short review on the wetting of liquid on planar surface. Wetting of liquid on solid surface is described by Young-Dupre' equation. The electrowetting on dielectric (EW) is described in detail using two basic approaches. In case of EW, the CA of liquid can be conveniently and reversibly changed just by external voltage. EW is noncontact and fast process and operates on simple capacitive design. Therefore it is used in many applications in optics and display devices. Also force imparted by the electric field on the droplet is used for transport, actuation, splitting, merging and mixing of the tiny amount of liquid inside micro-fluidic channel. It is also used in the physical characterization of

the liquid including interfacial tension and rheology.

Acknowledgment: One of the authors AGB would like to acknowledge BCUD, SPPU for research funding. Also YBS, would like to acknowledge UCG for fellowship.

References:

1. T. Young, Philos. Trans. Roy Soc. London 95, 65 (1805).
2. P.G. de Gennes, F. Brochard-Wyart, and D. Quere, Capillary and Wetting Phenomenon: Drops, Bubbles, Pearls, Springer: New York (2004).
3. G. Karapetsas, K. C. Sahu, K. Sefiane and O. K. Matar, Langmuir 30 (15), 4310-4321 (2014).
4. B. Yan, J. G. Tao, C. Pang, Z. Zheng, Z. X. Shen, C. H. A. Huan and T. Yu, Langmuir 24 (19), 10569-10571 (2008).
5. F. Mugele and J. C. Baret, J Phys-Condens Mat 17 (28), R705-R774 (2005).
6. G. Lippmann, Ann. Chim. Phys. 5, 495 (1875).
7. M. Vallet, B. Berge and L. Vovelle, Polymer 37 (12), 2465-2470 (1996).
8. B. Berge and J. Peseux, Eur Phys J E 3 (2), 159-163 (2000).
9. R. A. Hayes and B. J. Feenstra, Nature 425 (6956), 383-385 (2003).
10. J. Heikenfeld and A. J. Steckl, Appl Phys Lett 86 (15) (2005).
11. A. G. Banpurkar, K. P. Nichols and F. Mugele, Langmuir 24 (19), 10549-10551 (2008).
12. A. G. Banpurkar, M. H. G. Duits, D. van den Ende and F. Mugele, Langmuir 25 (2), 1245-1252 (2009).

-
13. R. B. Fair, *Microfluid Nanofluid* 3 (3), 245-281 (2007).
 14. L. D. Landau and E. M. Lifshitz, Pergamon Press LTD. Vol. 8 (1963).
 15. H. J. J. Verheijen and M. W. J. Prins, *Langmuir* 15 (20), 6616-6620 (1999).
 16. E. Seyrat and R. A. Hayes, *J Appl Phys* 90 (3), 1383-1386 (2001).
 17. N. B. Crane, A. A. Volinsky, P. Mishra, A. Rajgadkar and M. Khodayari, *Appl Phys Lett* 96 (10) (2010).
 18. B. Bhushan and Y. L. Pan, *Langmuir* 27 (15), 9425-9429 (2011).
 19. Y. Y. Lin, R. D. Evans, E. Welch, B. N. Hsu, A. C. Madison and R. B. Fair, *Sensor Actuat B-Chem* 150 (1), 465-470 (2010).
 20. R. Shamai, D. Andelman, B. Berge and R. Hayes, *Soft Matter* 4 (1), 38-45 (2008).
 21. <http://www.varioptic.com/>.
 22. <http://www.liquavista.com/>.
 23. K. Mishra, C. Murade, B. Carreel, I. Roghair, J. M. Oh, G. Manukyan, D. van den Ende and F. Mugele, *Sci Rep-Uk* 4 (2014).
 24. C. U. Murade, D. van der Ende and F. Mugele, *Opt Express* 20 (16), 18180-18187 (2012).
 25. R. de Ruiter, A. M. Pit, V. M. de Oliveira, M. H. G. Duits, D. van den Ende and F. Mugele, *Lab Chip* 14 (5), 883-891 (2014).
 26. G. Manukyan, J. M. Oh, D. van den Ende, R. G. H. Lammertink and F. Mugele, *Phys Rev Lett* 106 (1) (2011).
 27. A. Russell, E. Kreit and J. Heikenfeld, *Langmuir* 30 (18), 5357-5362 (2014).
 28. F. Mugele, *Soft Matter* 5 (18), 3377-3384 (2009).
 29. A. Quinn, R. Sedev and J. Ralston, *J Phys Chem B* 109 (13), 6268-6275 (2005).
 30. A. G. Papathanasiou and A. G. Boudouvis, *Appl Phys Lett* 86 (16) (2005).
 31. A. G. Papathanasiou, A. T. Papaioannou and A. G. Boudouvis, *J Appl Phys* 103 (3) (2008).
-

PIEZOELECTRICITY : A NEW WAY OF TAMING ENERGY

Mukesh Kumar¹ and Divakar Parashar²

^{1,2} Department of Physics

Swami Shraddhanand College, University of Delhi
Delhi 110036, India.

(Submitted: 17-10-2014)

Abstract

Recent globalization of Indian market loaded with a heavy dose of communism and have caused and credited speedy transport of heavy vibrations over and inside of highway surface. The energy radiated from these vibrations goes dissipated or wasted into surroundings and may be a cause of environmental pollution (apparent or hidden) wasted. In this paper we intended to tap and harness this energy of vibrations and wish to identify, scrutinize and devise ways so that a possible methodology could be developed. Vehicles on the highways that is spread across our whole country/land. This high speed of heavy vehicle necessarily exerts intense

1. Introduction

In recent times, there has been a soaring necessity of harvesting energy from various possible resources. It is the practice of acquiring energy from the environment which is being sent into trash and taming it for use wherever we needs.

Energy has always been regarded as a valuable diamond for the development of economy and is central to social growth of the country. There are two long-term energy challenges are being faced. One of them is undertaking climate change by mitigating Carbon Dioxide (CO₂) emissions and the other one is ensuring to secure clean and affordable energy.

Recently, the prices of petroleum based products are growing like ripple, which also affects our eating items. There is no way to negotiate with petroleum price hike. Besides, petroleum is like a good omen as well as a min giant for us.

Therefore, an alternative method to produce electricity has to be put in place.

Among other solutions which can be explored are nuclear and hydroelectric power generators. Besides, not every independent country is allowed to have the coolness of these power generators due to world political scenario. Thus, photovoltaic cells and wind turbines have been the popular choices and these renewable energy sources are gaining more attention. However, these options are much expensive and you should be a spendthrift to maintain them. As a consequence other possible energy sources need to be explored. Energy can also be harvested from ambient environment such as mechanical, thermal, light, electromagnetic and also human body to replace traditional sources.

Generally, the energy harvesting procedure include capturing of energy (resources), storing of

energy using batteries or other kind of capacitors, and finally the energy will supply power to nearby grid or system as shown in **Figure**



There are various forms of recycling of energy which have existed so far like:-

- Electrochemical Conversion
- Photovoltaic Panels
- Turbines
- Solar Cells
- Piezoelectricity

Energy Harvesting for Road Application^[4]

We introduces a new concept of energy recycling using the vibrations produced by the moving vehicles on the road and a transducer known as *piezoelectric transducer*. This method can be best utilized for efficient recycling of energy if we make use of this in a proper way. Vehicles such as cars, bus, trucks are the major user on the road. When every vehicle is in motion, it always will release energy in form of force or vibration direct to the road surface. An energy taming system will capture all these energies and convert it into electrical energy.

what is piezoelectricity ?

Discovered by J and P Curie in 1880, this is the method of converting mechanical energy into electrical energy. The piezoelectric effect exists in two domains, the direct piezoelectric effect that describes ability of material to convert mechanical strain into electrical energy, and its inverse effect, which is the ability of material to transform an applied electrical potential into mechanical strain.

ASA

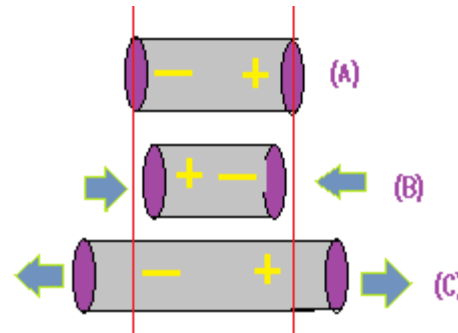


fig.1 (a) piezoelectric material with net dipole moment in horizontal direction (b)&(c) direct piezoelectric effect, any compression or tension generates an emf in the closed circuit

How to use energy from roads^[4]

The installation of piezoelectric sensors beneath the road surface which would produce electricity by using the vibrations caused by the movement of vehicles, is what our design proposes. This works in this way: the motion of a moving vehicle over pavement produces vibrations in the road surface which are being absorbed by a piezoelectric transducer. By installing relatively inexpensive and efficient piezoelectric transducer beneath the road surface, the vibrations transferred by vehicles can be converted into electricity.

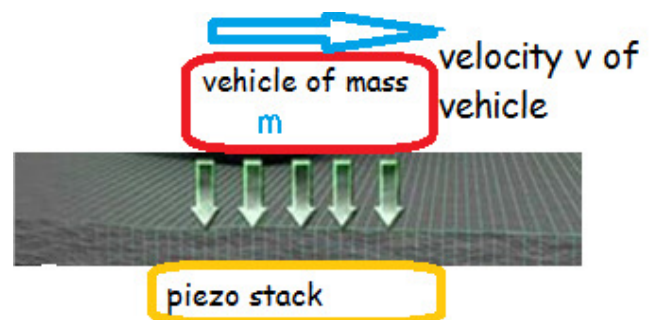


fig 2 : velocity of the vehicle is in horizontal direction and energy transferred to the piezo stack is in downward direction

2. Mathematical Treatment

The energy generated can be calculated by assuming this model in two parts: mechanical model and electrical model.^[5]

Mechanical Model

It consists of one or more piezoelectric elements between two heavy masses. This is known as Piezo stack. Consider a vehicle, of mass **m**, passes over this piezo stack, there will be a slightly decrease in the potential energy of the vehicle due to the deformation in the road. This changed potential energy is transferred into the piezo stack.

Here **mg** will be known as deforming factor and will be responsible for amount of deformation in the piezo stack, **g** being because of earth's gravitational field.

Let Δl is the deformation produced in the piezo stack. Thus change in potential energy of the vehicle is given by **mg Δl** .

Δl depends on two factors

- elastic properties of the piezoelectric element
- mass, **m**, of the vehicle

Consider that the piezo stack having thickness **h** and area of cross section **A**, the Young's modulus for this stack is defined by :

$$Y = \frac{(mg)h}{\Delta l \cdot A}$$

or $\Delta l = (mg) \cdot \frac{h}{YA}$

the energy transferred to the stack is, therefore

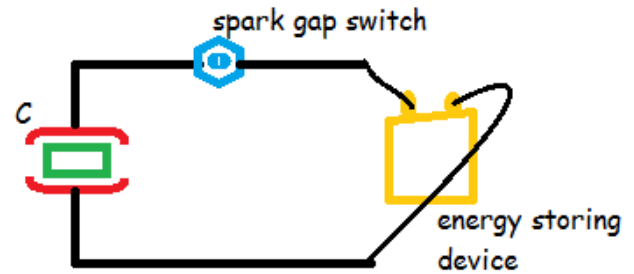
$$E_t = m \cdot g \cdot \Delta l$$

or, $E_t = (m \cdot g)^2 \cdot \frac{h}{YA}$

Where E_t is the energy transferred to the piezo stack by the moving body.

Electrical Model

Let us consider the case(ideal condition) when the whole energy lost by the vehicle is transferred to the piezo stack, and it converts all the energy transferred to it into the electrical energy. The piezoelectric element is a metalized dielectric material which is analogous to a capacitor.



Capacity of the stack is given by

$$C = \frac{\epsilon_r \cdot \epsilon_0 \cdot A}{h}$$

ϵ_0 is absolute permittivity of free space, ϵ_r is relative permittivity of material which the piezo stack is made up of

If **V** is the voltage generated as a result, the energy stored in the capacitor is given by

$$E = \frac{1}{2} \cdot CV^2$$

This stored energy in the capacitor is the energy transferred to the piezo stack because of the change in the potential energy of the moving mass. Therefore, the electrical energy produced and change in potential energy of the vehicle should be equal to each other, that we have formulated earlier.

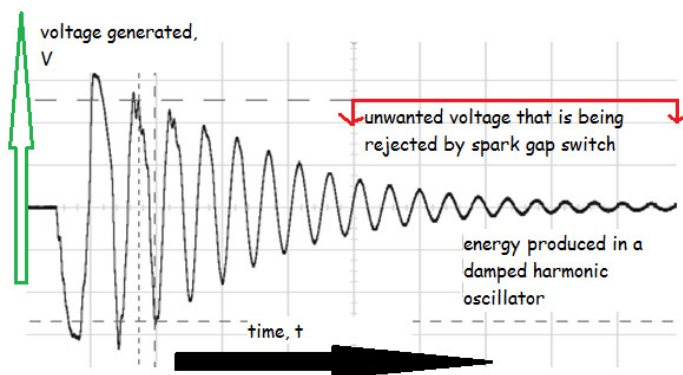
$$E = E_t$$

$$\frac{1}{2} \cdot CV^2 = (m \cdot g)^2 \cdot \frac{h}{YA}$$

$$V^2 = (m \cdot g)^2 \cdot \frac{\epsilon_0 \cdot \epsilon_r}{Y}$$

or, $V = m \cdot g \sqrt{\left\{ \frac{\epsilon_r \epsilon_0}{Y} \right\}}$

All other quantities except mass will remain constant for a particular piezoelectric element. Thus the voltage generated depends directly on mass, greater is the mass of the moving body larger is the voltage generated. Since the velocity is in horizontal direction and the force responsible for generation of electricity is in vertically downward direction, the velocity of the moving body, therefore, will not leave any impact on the energy produced, except the contact time will be decreased on increase of velocity which will result in changed frequency of the current generated. The piezo stack will continue to oscillate even after the vehicle has passed over it, therefore damped harmonic motion will occur in the piezo stack. The energy of damped harmonic decreases as shown in fig . That's why we use a spark gap switch to reject the unwanted amount of voltage.



2. Results and Discussion

According to law of conservation of energy, energy can neither be created nor be destroyed, only transferred from one form to another. This is the same phenomena that is applied in this paper by capturing the energy wasted by the vehicle in the form of transferred vibrations and converting it into electrical energy, storing it and making useful for various purpose. Theoretical results shows that a large part of energy that is being wasted can be tamed and used for various purposes. A report^[4]

based on a project in Japan, shows that a considerable amount of electrical energy was generated after installation of piezoelectric transducers at the busiest railway station of Japan. Not the all the energy dissipated by the vehicle is made useful, most of the energy gets demolished during the process and output power is very low about 0.0018 kW/km for 45,000 N truck weight.[2]

Berkeley Result	Modified Berkeley Calculation	Virginia Tech Demonstration
600 trucks per hour	600 trucks per hour	As low as 167 vehicles per hour
45,000 N tuck weight	147,000 N truck weight, tractor trailer	Tractor trailer
8 axles per truck	tractor trailer, 5 axles	5 axles
0.0018kW/km, <1mW at the module	0.01 kW/km, 0.017 W/module	0.08-0.14 W per module

Table1: Comparison of Calculation Results across Multiple Third-Party Investigators into the Compression-Based Energy Harvesting Technology[2]

The report discussed above is not only the work that has been done. Many others has done a significant work in this field and others are trying to find new possibilities that can increase the efficiency and make it useful for every aspect of life.

Limitations and Scope

1. The vibrations have to transfer through the material of which the road surface is made up of. In this case there will always be **structural damping** which leaves impact on the amount of electrical energy generated.

2. Consider the case of appearance of charge. Let n number of electrons transfer because of applied force \mathbf{f} (or $\mathbf{m.g}$). For a particular value of force the charge generated will be the same. It will depend on the structure of the crystal of piezoelectric element or the dipole strength of the crystal. But every crystal has a critical value of mass over which it will possess only a slightly change in the value of electrical energy generated, even on the great change in force applied, or in other words change in mass of the body.

3. Not all the energy dissipated by the vehicle is made useful, most of the energy get demolished during the process and output power is low.

References :

[1] Arjun A.M., Ajay Sampath, Sandhya Thiagarajan, and Arvind V, *International*

Journal of Environmental Science and Development, Vol. 2, No. 6, December 2011

[2] Cost of Energy and Demonstration Roadmap, Prepared by: DNV KEMA Energy & Sustainability

[3] Foot step power generation using piezoelectric material, www.BEProjectReport.com

[4] Kamarul Faiz bin Mihaj, Dr. Kok Boon Ching, *Dalam Pendidikan Dan Latihan Teknikal Dan Vokasional (CiE-TVET 2013)*

[5] Kshitiz Upadhyay and Anup Shanker, *Indian Journal of Applied Engineering and Technology* Vol-2(1), 2012

Magneto-caloric Effect and Magnetic Field Induced Strain of Heusler Alloys

Mrittunjoy Guha Majumdar¹

¹Department of Physics
University of Cambridge
Cambridge, UK.

(Submitted: 10-10-2012)

Abstract

Heusler Alloys are alloy compounds with the molecular formula X_2YZ , where X and Y are transition-series elements and Z is from the s or p group. They are found to be of immense significance due to certain characteristics such as shape memory, half-metal nature and the Magneto-Calorific Effect (MCE). In this short summer-project that I was involved in at the Indian Institute of Technology, I studied the MCE effect in Heusler Alloys using a Vibrating Sample Magnetometer (VSM) and the Calorimeter.

1. Shape Memory

Shape Memory, as the name suggests, is the tendency of a body to assume a certain form upon variations of external conditions such as temperature. It usually refers to the tendency of a body to “remember” its original form before deformation and transition by heating. There are two forms of structure in such compounds: the Martensite and Austernite forms. The physical understanding of shifts between the two forms can be thought of in terms of the molecular lattice structure in case of Shape Memory Alloys (SMA). Such compounds usually assume the L21 lattice structure that has 4 interpenetrating FCC unit cells.

Martensite is a crystal structure that is formed by displacement transformation, as

opposed to the common diffusive transformations, which is much slower. For reversible martensitic transformation to occur, the following conditions must be satisfied:

1. the driving force for the transformation should be small
2. the interface between the martensite and the austenite phases has to be mobile upon heating and cooling
3. the transformation should be crystallographically reversible.

Martensitic transformations are usually first order solid state structural phase transitions. The atoms move in an organized manner relative to their neighbors and therefore they are known as ‘military’ transformations in contrast to diffusion-based ‘civilian’ transformations. And the displacement can

be described as a homogeneous lattice deformation.

The temperature ranges over which the Martensite and the Austernite states exist are defined by M_s and M_f temperatures (Start temperature and Finish temperature for Martensite phase) and similarly, the T_s and T_f temperatures for the Austernite phase. The cycle over which SMAs change from the Martensite phase to the Austernite phase by the application of heat and then from the Austernite phase to the Martensite phase by rapid cooling is characterized by a hysteresis curve with a loss of energy as heat.

Upon application of heat, lattice structures change. For instance, if the Martensite structure has a cubic structure, upon heating, the lattice points may extend in a single direction to give a tetragonal shape in the Austernite phase. Such shape ‘memories’ may be unidirectional (where the body tends to retake its shape in either of the phases and never in the other) or bidirectional.



2. Magnetic Entropy (S_m)

Entropy refers to the disorderliness of a system, in terms of state variables of its constituent entities. As shown in the illustration. A ferromagnetic material (Fig 2.a) has strong magnetization in the direction of the external magnetic field. An anti-ferromagnetic material has equal magnetization in the direction and opposite to the direction of the magnetic field.

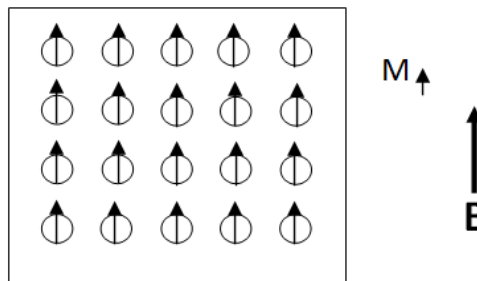


Fig 2.a

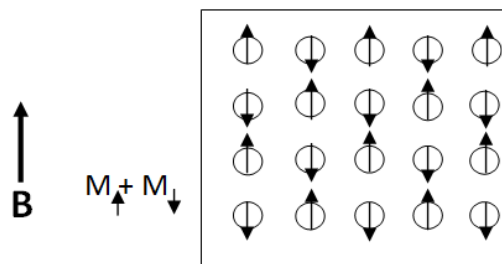


Fig 2.b

For anti-ferromagnetic material, M_{\downarrow} and M_{\uparrow} exactly nullify each other. However, in ferromagnetic materials, there is some net magnetization in one of the directions. In Heusler alloys, the constituents of the alloy define the magnetic character of the alloy. The table below shows some examples of Heusler Alloys and their magnetic properties.

Heusler Alloy	Magnetic Character
Mn_2VAl	Ferrimagnetic
Fe_2VAl	Non-Magnetic
Co_2MnSi	Ferromagnetic

By changing from one state with a certain magnetic property to another state with a different distinct property, we are bringing in magnetic entropy changes. By partial doping of certain elements in a Heusler Alloy, the magnetic character can be manipulated.

Now, given that there is entropy associated with such systems, one can associate heat evolved as entropy changes take place. This heat evolved is the result of what is termed as Magneto-Calorific Effect.

3. Ferromagnetic Shape-Memory Alloys (FSMAs)

The idea of temperature-dependent shape-memory can be extended to magnetic-field dependent FSMA shape-memory. One can think of the physical picture in terms of alignment of domains upon the application of external magnetic field. This property of the FSMAs is often used to generate Magnetic Field Induced Strain (MFIS), which can be applied in various ways such as in electric circuit switches.

4. Half-Metallic Nature of Heusler Alloys

Heusler Alloys display half-metallic character.

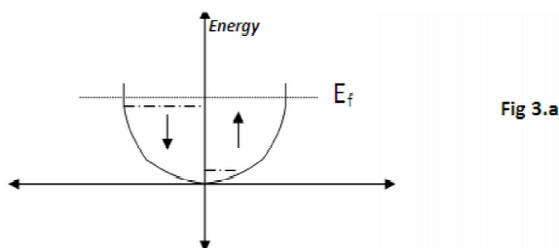


Fig 3.a

In general, the number of spin-up electrons and spin-down electrons are same and upon application of same and upon application of external magnetic field, some of the external magnetic field, some of the electrons in one of the states electrons in one of the states (depending upon the direction of field) are shifted from one spin state to the other, as

shown in Fig 3.a. In these materials the two spin bands these materials the two spin bands show a completely different behavior. While the majority spin band (referred also as spin-up band) shows the typical metallic behavior, the minority spin band (spin band) exhibits a semiconducting behavior with a gap at the Fermi level. Therefore such half ferromagnets and can be considered as hybrids between metals and semiconductors. This has been ferromagnets and can be considered as hybrids between metals and semiconductors. This has been ferromagnets and can be considered as hybrids between metals and semiconductors. This has been illustrated in Fig 3.b.

But for half-magnetic behavior, we have the energy profile for spin-states as shown in Fig 3.b. As can be seen there is a distinct band-gap between the localized energy profiles for the spin-up state in the graph. This marks the fully-polarized state that I exploited as the half-magnetic property.

Adding the spin degree of freedom to the conventional electronic devices has several advantages like non-volatility, increased data processing speed and decreased power consumption. The current advances in new materials speed and especially in the metals are promising for engineering new spintronic devices in the near future.

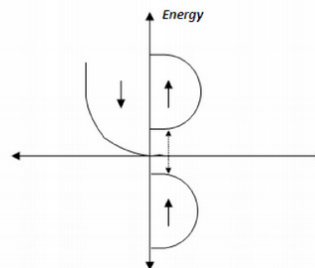


Fig 3.b

5. Magnetic Field Induced Strain (MFIS)

The MFIS phenomenon is seen in Heusler Alloys. The physical understanding of this effect can be found in the structural changes effected by magnetization in a lattice. It can be thought of as the structural changes effected by magnetization in a lattice. It can be thought of as a giant the structural changes effected by magnetization in a lattice. It can be thought of as a magnetostrictive effect. Dimensional changes of 10% have been realized with Magnetic Field Induced Strain.

6. Magneto-Calorific Effect

The mathematical treatment of the MCE effect has been studied:

The internal energy of a system can be represented either as $U = U(S, V, H)$ or $U = U(S, V, M)$ where M is the Magnetic Moment, H is the Magnetic Field, S is the Entropy and V represents the Volume. Correspondingly the differential dU can have the forms:

$$dU = TdS - pdV - MdH \text{ or } dU = TdS - pdV - HdM \quad \dots(1)$$

The *Free Energy (F)*, which is a function of Temperature, Volume and Magnetic Field (H), is used for systems with constant volume and is defined as $F = U - TS$. Its differential is given by

$$dF = -SdT - pdV - MdH \quad \dots(2)$$

The *Gibbs Free Energy (G)* is a function of Temperature, Pressure and Magnetic Field (H) and is used for systems under constant pressure. It is defined as $G = U - TS + pV - MH$. Its differential is given by

$$dG = -SdT + Vdp - MdH \quad \dots(3)$$

For the free energy F the internal parameters Entropy, Pressure and Magnetic Moment (M), conjugated to the external variables Temperature, Volume and Magnetic Field (H), can be determined by the following equations of state

$$S(T, H, V) = - \left(\frac{\partial F}{\partial T} \right)_{H, V} \quad \dots(4)$$

$$M(T, H, V) = - \left(\frac{\partial F}{\partial H} \right)_{T, V} \quad \dots(5)$$

$$p(T, H, V) = - \left(\frac{\partial F}{\partial V} \right)_{H, T} \quad \dots(6)$$

Analogously, we have

$$S(T, H, p) = - \left(\frac{\partial G}{\partial T} \right)_{H, p} \quad \dots(7)$$

$$M(T, H, p) = - \left(\frac{\partial G}{\partial H} \right)_{T, p} \dots\dots\dots (2) \quad \dots(8)$$

$$V(T, H, p) = \left(\frac{\partial G}{\partial p} \right)_{H, T}$$

...(9)

$$\alpha_T = -\frac{1}{V} \left(\frac{\partial S}{\partial p} \right)_{H,T}$$

Using (4) – (9),

...(16)

$$\left(\frac{\partial F}{\partial T} \right)_{H,V} = \left(\frac{\partial G}{\partial T} \right)_{H,p}$$

...(10)

Now, $dS = \left(\frac{\partial S}{\partial T} \right)_{H,p} dT + \left(\frac{\partial S}{\partial H} \right)_{T,p} dH + \left(\frac{\partial S}{\partial p} \right)_{H,T} dp$

$$\left(\frac{\partial F}{\partial H} \right)_{T,V} = \left(\frac{\partial G}{\partial H} \right)_{T,p}$$

...(11)

...(17)

$$\left(\frac{\partial F}{\partial V} \right)_{H,T} = - \left(\frac{\partial G}{\partial p} \right)_{H,T}$$

...(12)

Using equations (10), (15), (16) and (17), and setting $dS = 0$ for an adiabatic process,

$$\frac{C_{H,p}}{T} dT + \left(\frac{\partial M}{\partial T} \right)_{T,p} dH - \alpha_T V dp = 0$$

...(18)

The Heat Capacity C_x at constant variable x is defined by

$$C_x = \left(\frac{\partial Q}{\partial T} \right)_x$$

...(13)

where $C_{H,p}$ is the heat capacity under constant magnetic field and pressure.

where δQ is the heat quantity changing the system temperature on dT . By IInd Law of Thermodynamics,

$$\delta S = \frac{\partial Q}{T}$$

...(14)

Under an *adiabatic–isobaric process* ($dp = 0$, this process is usually realized in Magnetocaloric experiments) the temperature change due to the change of the magnetic field (the Magnetocaloric effect) can be obtained as

$$dT = -\frac{T}{C_{H,p}} \left(\frac{\partial M}{\partial T} \right)_{H,p} dH$$

...(19)

$$C_x = T \left(\frac{\partial S}{\partial T} \right)_x$$

...(15)

Now, defining the Bulk Modulus κ as

$$\kappa = -\frac{1}{V} \left(\frac{\partial V}{\partial p} \right)_{T,H}$$

The bulk thermal expansion coefficient can be represented by $\alpha_T = \alpha_T(T, H, p)$. Since

$$\alpha_T V = \left(\frac{\partial V}{\partial T} \right)_{H,p}$$

For an *adiabatic–isochoric process* ($dV = 0$) the total differential dV has the form

$$dV = \alpha_T V dT + \left(\frac{\partial V}{\partial H} \right)_{T,p} dH - \frac{V}{\kappa} dp = 0$$

...(20)

and equation (11) applies,

Using (18) and (20),

$$\left[\frac{C_{H,p}}{T} - \alpha_T^2 \kappa V \right] dT + \left[\left(\frac{\partial M}{\partial T} \right)_{H,p} - \alpha_T \kappa \left(\frac{\partial V}{\partial H} \right)_{T,p} \right] dH = 0$$

The second term is found to be small and thus can be neglected.

Hence, the equation of Magnetostriction Effect is given by

$$dT = - \frac{T}{C_{H,p}} \left[\left(\frac{\partial M}{\partial T} \right)_{H,p} - \alpha_T \kappa \left(\frac{\partial V}{\partial H} \right)_{T,p} \right] dH$$

Where, the second term is due to the internal magnetostrictive tensions arising from the change in magnetic state of the system keeping the volume constant. This way one can see that change of magnetization with temperature leads to heating or cooling.

One can analyze the various cases for the given equation.

1. If $C_{H,p}$ is high, the change in temperature will be low, which is true for the property of heat capacity.
2. If $\left(\frac{\partial M}{\partial T} \right)_{H,p} > \alpha_T \kappa \left(\frac{\partial V}{\partial H} \right)_{T,p}$ then heating occurs. For $\left(\frac{\partial M}{\partial T} \right)_{H,p} < \alpha_T \kappa \left(\frac{\partial V}{\partial H} \right)_{T,p}$ cooling occurs. If the magnetization produced for unit change in temperature is less than the internal magnetostrictive tensions used for keeping the volume constant, the heat generated will be used up for the latter and thus cooling occurs. A similar line of thought can be employed to argue for the case of heating.

3. The effect is stronger at higher temperatures (T) as can be observed in the equation.

Experimentation

Preparation of Samples

The process used for preparation of Heusler Alloy sample for analysis involves arc-melting, using which the alloy ingots were obtained. Elemental powders of Nickel (Ni), Gallium (Ga) and Manganese (Mn), as per the target composition, are weighed in a calibrated electronic balance and blended thoroughly. The blended alloy mixture is cold-compacted in a stainless steel die under a pressure of 40 Mega-Pascal.

The compacted pellet is placed in the water-cooled copper hearth of the arc furnace and the chamber is pumped down to around 10^{-5} Torr.

The chamber is purged with Argon gas to remove traces of oxidizing atmospheric gases and finally filled with argon gas pressure of 750 Torr. A DC arc is then struck and the pellet is melted. The cast ingot is then flipped around and re-melted 3-4 times to ensure complete melting of the constituent elements.

The alloys thus obtained are brittle and also need to be homogenized further to obtain samples with consistent properties. The metallic ingots cannot be heat treated in air since they might oxidize. So, the as-cast ingots are taken separately in fused silica ampoules, which are pumped down to 10^{-5} Torr and then flame-sealed. The vacuum-sealed ampoules containing the alloy ingots are placed inside a raising hearth furnace, homogenized at 1423 K for 24 hours and allowed to slowly cool inside the furnace. The slowly cooled samples do not show any

signature of Martensitic transformations in Differential Scanning Calorimeter (DSC) studies. So, the cylindrical ingots are cut into small discs and cleaned with Acetone ($\text{CH}_3\text{—CO—CH}_3$) in an ultrasonic bath.

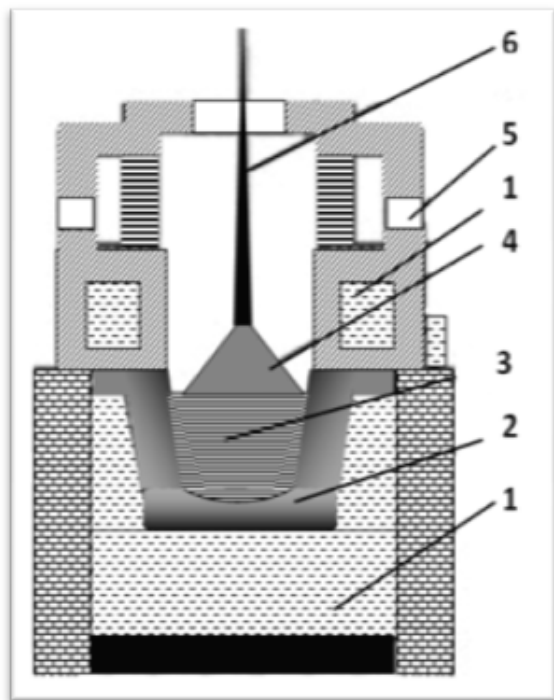


Figure: Labels

1. Circulating water to cool the hearth,
2. Copper hearth
3. Compacted metal blend
4. Electric arc struck between the electrodes
5. Gas inlet valve
6. Water cooled flexible electrode with tungsten tip (anode).

Figure 4

The dried discs are again flame-sealed in fused silica ampoules at a pressure of 10^{-5} Torr, annealed separately at various temperatures for 6 hours and quenched. Air, ice water and liquid nitrogen are used as quenching media for different investigations. Thick discs (8 mm thickness) are annealed at 1273 K and quenched in ice

water for mechanical testing (Stress - Strain studies).

Characterization

Differential Scanning Calorimeter (DSC)

Differential Scanning Calorimeter is a device used for thermo-analytic studies in which the difference in the amount of heat required to increase the temperature of a sample and a reference material is measured as a function of temperature.

The DSC curves are recorded either under a constant heating (or cooling) rate or under isothermal conditions. A typical DSC consists of two isolated sealed pans, one containing the sample and the other a reference material.

The two pans are heated or cooled uniformly while the heat flow difference between the two is monitored.

The basic principle underlying this technique is the following: when the sample undergoes a physical transformation such as phase transition, more or less heat will need to flow to it in comparison with the reference in order to maintain both at the same temperature.

In the power compensation type DSC, heat is supplied to either of the pans so that both are maintained at the same temperature. The heat flow (dH/dt) is then estimated from this data.

In a DSC based on the heat-flux technique, the temperature difference (ΔT) between the two isolated pans is measured from which the heat flow is estimated.

For a Shape-Memory Alloy such as a Heusler Alloy, the DSC curve obtained is shown in Figure 5. We can see distinct representation for the temperatures M_s , M_f , A_s and A_f .

during the solid state phase transformation from martensite to austenite, energy is absorbed by the system (endothermic reaction).

Similarly, during the transformation from austenite to martensite, energy is released from the system (exothermic reaction). The Gibbs free energy change of a system at $M \leftrightarrow A$ transformation may be written as,

$$\Delta G = \Delta G_c + \Delta G_s + \Delta G_e = \Delta G_{nc} + \Delta G_c$$

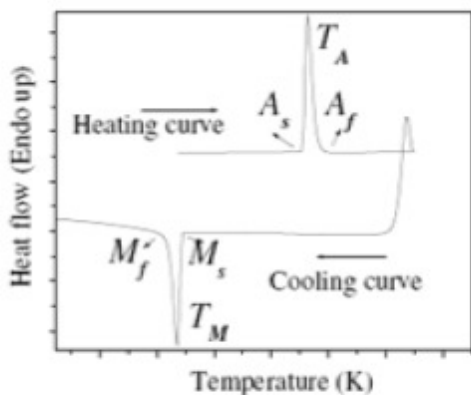
Where ΔG_c is a chemical energy term originating in the structural change from

parent to martensite and ΔG_{nc} is the non-chemical energy term contains a surface energy term (ΔG_s between austenite and

martensite) and elastic energy term (ΔG_e around the martensite).

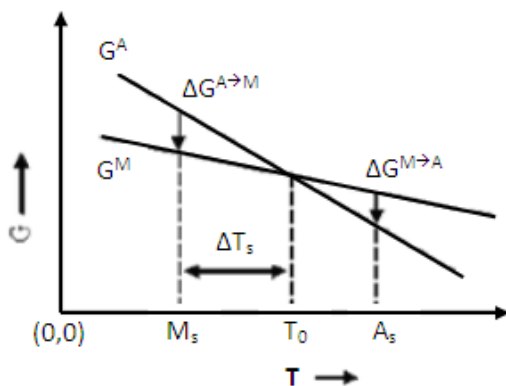
$$\Delta G_c = \Delta H - T_0 \Delta S = 0$$

In most martensitic transformations, ΔG_{nc} is equally large as ΔG_c . In the absence of elastic strain energy, the forward and reverse transformation temperatures (i.e. M_s and A_s) coincides with the thermodynamic equilibrium ($\Delta G = 0$) temperature T_0 .



- M_s : Martensite start temperature upon cooling
- M_f : Martensite finish temperature upon cooling
- T_M : Martensite peak temperature upon cooling
- A_s : Reverse transformation start temperature upon heating
- A_f : Reverse transformation finish temperature upon heating
- T_A : Reverse transformation peak temperature upon heating

Figure 5



The free energy of the martensite phase is more than that of the austenite phase. Thus,

This non-chemical energy term changes the driving forces and hence T_0 . A further supercooling of ΔT_s from T_0 is necessary for inducing the Martensitic transformation and superheating is necessary for the reverse Martensitic transformation.

The fact that the Martensitic Start and Finish temperatures are not the same can be explained in a similar way. Elastic energy around the martensite resists the growth of the martensite unless a further driving force such as cooling is performed on the system.

Vibrating Sample Magnetometer (VSM)

The VSM is used usually for studying Hysteresis Curves, where the dependence of magnetic moment of a sample to the external magnetic field is analyzed.

For studying the Magnetocaloric Effect, we study the magnetization as a function of temperature.

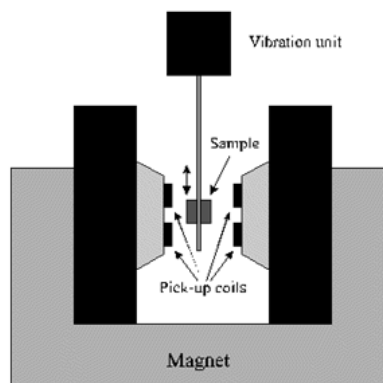


Figure 6

A sample is placed inside a uniform magnetic field to magnetize the sample. The sample is then physically vibrated, typically through the use of a piezoelectric material. The induced voltage in the pickup coil is

proportional to the sample's magnetic moment. It, however, does not depend on the strength of the applied magnetic field. In a typical setup, the induced voltage is measured through the use of a lock-in amplifier using the piezoelectric signal as its reference signal.

One expects to observe a curve that comprises of two kinds of transformation: Ferromagnetism-to-Paramagnetism and Austenite-to-Martensite. The former is represented in an M vs. T graph as the dip in the curve profile at the Curie temperature. For the latter, hysteresis is observed in the curve besides the appearance of peaks in the regions between A_s and A_f , and between M_s and M_f . The hysteresis can be explained by considering that for phases such as the Martensitic phase, the lattice-units are held in position by the surrounding lattice structure in such a manner that a greater energy is needed to bring about an appreciable change in the magnetization than for the Austenitic phase. In other words, the heat lost, represented in the curve area, is used up for the transformation.

However, in some cases, as in our sample, the transformation temperature and the Curie temperature are very near each other. In such a case, the peaks observed at transformation temperatures disappear. We only obtain a smooth decline in the curve although hysteresis is present, implying a first order transition in the state.

Strain Gauge

The strain gauge has been used for studying the Magnetic-Field Induced Strain (MFIS) in $\text{Ni}_{50}\text{Mn}_{30}\text{Ga}_{20}$ alloy. A Strain Gauge

essentially works on the principle of variation of resistance due to change in the strain in the Gauge. Usually, it constitutes an arm of a Wheatstone Bridge that, because of the change in strain, leads to a visible change in the balancing condition.

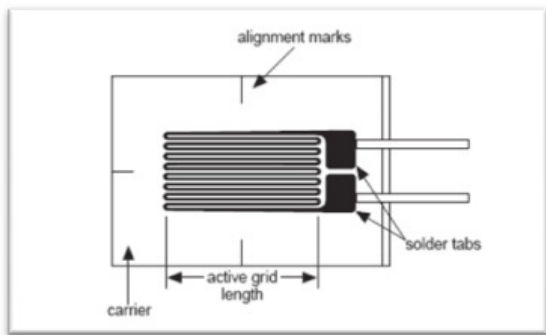


Figure 7

The metallic strain gauge consists of a very fine wire or, more commonly, metallic foil arranged in a grid pattern. The grid pattern maximizes the amount of metallic wire or foil subject to strain in the parallel direction. The grid is bonded to a thin backing, called the carrier, which is attached directly to the test specimen.

A fundamental parameter of the strain gauge is its sensitivity to strain, expressed quantitatively as the gauge factor (GF). Gauge factor is defined as the ratio of fractional change in electrical resistance to the strain developed.

$$Gauge\ Factor = \frac{\Delta R/R}{\Delta l/l}$$

For my study, the Gauge factor on the catmanEASY interface was set to 2.

The general Wheatstone bridge, illustrated below, consists of four resistive arms with

an excitation voltage, V_{exc} that is applied across the bridge.

$$V_0 = \left[\frac{R_3}{R_3 + R_4} - \frac{R_2}{R_2 + R_1} \right] V_{exc} \dots\dots\dots(S)$$

If we replace any of the arms of a balanced Wheatstone bridge with a Strain Gauge and introduce strain in it, we get an unbalanced bridge. If the nominal resistance of the Gauge is R_G then the change in resistance due to strain can be expressed as

$$\Delta R = R_G * Gauge\ Factor * Strain$$

Now putting $R_1 = R_2$, $R_3 = R_G$ and $R_4 = R_G + \Delta R$ (initially, before strain is applied, $R_4 = R_G$) in (S)

$$\frac{V_0}{V_{exc}} = \frac{Gauge\ Factor * Strain}{1 + \frac{Gauge\ Factor * Strain}{2}}$$

In this experiment, we firstly have to do the calibration for the Strain Gauge. For this, I took a reference sample that had predetermined values for Strain for given values of external magnetic field.

After this, the data for the sample is taken and the calibration is used to get the final calibrated value. The interface used, for my study, was catmanEASY with a Strain Gauge 120 Ω Transducer with a Bessel Filter of 5 Hz and Gauge Factor of 2. The Excitation Voltage was kept at 5 V.

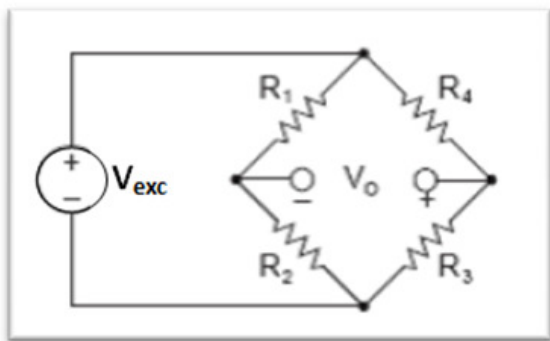


Figure 8

The expected result is the development of, and increase in, strain with increasing magnetic field. The highest strain developed in the alloy-system being studied that has been reported is 10%. However, the strain developed can be due to compression or elongation as per the material's behavior towards a given external magnetic field.

Conclusion

Shape Memory, Magnetic Field-Induced Strain (MFIS) and Half Metallic Nature of Heusler Alloys were studied. The Magnetocaloric effect is analyzed and the governing equation is derived.

Experimental methods are explored. The techniques for preparation and characterization of Heusler Alloys are studied.

Acknowledgements

I would like to acknowledge the contribution of Dr. Ananthkrishnan Sreenivasan (*Department of Physics, Indian Institute of Technology, Guwahati*) in guiding me during this study of Heusler Alloys. I would also like to acknowledge the contribution of

Mr. Rahul Das, Ms. Nisha Shankhwar, Mr. Bhargab Deka and Mr. Arnab Kumar Das whose guidance was of utmost importance for understanding the experimental techniques of preparation and characterization of Heusler Alloys.

References

- [1] A. M. Tishin, Y. I. Spichkin. *The Magnetocaloric Effect and Its Applications* by and, Institute of Physics *Series in Condensed Matter Physics*, IOP Publishing Ltd (2003).
- [2] C. Jiang et al, *Composition dependence on the martensitic structures of the Mn-rich NiMnGa alloys*, *Acta Materialia*, 52 (2004) 2779-2785.
- [3] K. Oikawa et al, *Magnetic and Martensitic Phase Transformations in a Ni₅₄Ga₂₇Fe₁₉ Alloy*, *Materials Transactions*, Vol. 43, No. 9 (2002) pp. 2360 – 2362.
- [4] I. Galanakis and P. H. Dederichs, *Half-Metallicity and Slater-Pauling Behavior in the Ferromagnetic Heusler Alloys*, *Notes Phys.* 676, 1–39 (2005).
- [5] Podmiljsak, Benjamin, et al. *Magnetocaloric properties and nanoscale structure of Fe-doped Gd₅Ge₂Si₂ alloys*. *Journal of Applied Physics* 105.7 (2009): 07A941-07A941.

Squaring and Cubing of Binary Numbers

M.N.MURTY

Department of Physics, National Institute of Science and Technology,

Berhampur-761008, Odisha, India.

e-mail: mnarayanamurty@rediffmail.com

(Submitted: 25-07-2014)

Abstract

The book on 'Vedic Mathematics' written by Jagadguru Sankaracarya Sri Bharati Krisna Tirthaji Maharaja contains 16 Sutras or formulas and 13 Sub-Sutras or corollaries to carry out various arithmetical operations. The sutra 'Urdhva Tiryagbhyam' is used for multiplication of two decimal numbers containing equal number of digits. The squaring of a binary number can be done using this sutra. The sub-sutra 'Anurupyena' is used to find the cube of a decimal number. The cube of a binary number can be evaluated using this sub-sutra. The multiplication of binary numbers is used in the field of digital signal processing for the design of digital multipliers.

1.Introduction

The book on 'Vedic Mathematics' written by Jagadguru Sankaracarya Sri Bharati Krisna Tirthaji Maharaja was first published in 1965. It contains 16 Sutras or formulas and 13 Sub-Sutras or corollaries to carry out various arithmetical operations. The meaning of the sutra 'Urdhva Tiryagbhyam' is vertically and cross-wise. This sutra is used for multiplication of two decimal numbers containing equal number of digits. The squaring of binary numbers can be done using this sutra. The sub-sutra 'Anurupyena' is used for cubing a decimal number. This sub-sutra can be used for finding the cube of a binary number. A large amount of

research work has so far been done for understanding these sutras.

The multiplication of binary numbers is used in the field digital signal processing for the design of digital multipliers. The speed of a digital signal processor is largely determined by the speed of its multipliers. The squaring operation also forms the backbone in cryptography.

The rest the paper is organized as follows. Multiplication of two decimal numbers using 'Urdhva Tiryagbhyam' sutra is given in Section 2. In Section 3, the squaring of a binary number using this sutra is given. The multiplier based on 'Urdhva Tiryagbhyam' sutra for squaring a 2-bit binary number is presented in Section 4. The cubing of a decimal number using the sub-sutra

‘Anurupyena’ is given in Section 5. In Section 6, the cubing of a binary number using this sub-sutra is discussed.

2. Multiplication of Two Decimal Numbers Using ‘Urdhva Tiryagbhyam’ Sutra

The meaning of the sutra ‘Urdhva Tiryagbhyam’ is vertically and cross-wise. This sutra is used for the multiplication of two decimal numbers containing equal number of digits. The multiplication of two decimal numbers basing on this sutra is illustrated in the following examples.

Example 1: Multiplication of two 2-digit decimal numbers 84 and 52.

Let the product of 84 and 52 is $P_3P_2P_1P_0$.

$$\begin{array}{r}
 84 \quad - \\
 \text{Multiplicand} \\
 \times 52 \text{ - Multiplier} \\
 \hline
 P_3P_2P_1P_0 \\
 \hline
 \end{array}$$

The multiplication of these numbers is carried out as per the following steps.

Step 1: Multiply the right-hand-most digit 4 of the multiplicand vertically by the right-hand-most digit 2 of the multiplier.

$$\begin{array}{r}
 4 \\
 \downarrow \\
 2 \\
 \hline
 4 \times 2 = \\
 8 \\
 \hline
 \end{array}$$

Step 2: Multiply 8 and 2, and 4 and 5 cross-wise. Add the products.

$$\begin{array}{r}
 8 \quad \quad 4 \\
 \swarrow \quad \searrow \\
 5 \quad \quad 2 \\
 \hline
 8 \times 2 + \\
 4 \times 5 = 36 \\
 \hline
 \end{array}$$

Step 3: Multiply the left-hand-most digit 8 of the multiplicand with the left-hand-most digit 5 of the multiplier.

$$\begin{array}{r}
 8 \\
 \downarrow \\
 5 \\
 \hline
 8 \times 5 = \\
 40 \\
 \hline
 \end{array}$$

Step 1: 8; 8 carry 0; $P_0 = 8$

Step 2: $36 + 0 = 36$; 6 carry 3; $P_1 = 6$

Step 3: $40 + 3 = 43$; 3 carry 4; $P_2 = 3$

Carry of *step 3* = $P_3 = 4$

Thus, the product is 4368.

Example 2: Multiplication of two 3-digit decimal numbers 395 and 746.

$$\begin{array}{r}
 395 \\
 \times 746 \\
 \hline
 P_5P_4P_3P_2P_1P_0 \\
 \hline
 \end{array}$$

The steps for multiplication are given below.

Example 3: Multiplication of two 4-digit decimal numbers 9731 and 4682.

<i>Step 1</i>	<i>Step 2</i>
$\begin{array}{r} 5 \\ \downarrow \\ 6 \\ \hline 5 \times 6 = \\ 30 \end{array}$	$\begin{array}{r} 9 \quad 5 \\ \swarrow \quad \searrow \\ 4 \quad 6 \\ \hline 9 \times 6 + \\ 5 \times 4 = 74 \end{array}$

9731	
9 5 × 4682	
$P_7 P_6 P_5 P_4 P_3 P_2 P_1 P_0$	_____ _____ _____

This multiplication is done as per the following steps.

<i>Step 3</i>	
$\begin{array}{r} 3 \quad 9 \quad 5 \\ \swarrow \quad \downarrow \quad \searrow \\ 7 \quad 4 \quad 6 \\ \hline 3 \times 6 + 9 \times 4 + 5 \times 7 = 89 \end{array}$	

<i>Step 1</i>	<i>Step 2</i>
$\begin{array}{r} 1 \\ \downarrow \\ 2 \\ \hline 1 \times 2 = 2 \end{array}$	$\begin{array}{r} 3 \quad 1 \\ \swarrow \quad \searrow \\ 8 \quad 2 \\ \hline 3 \times 2 + \\ 1 \times 8 = 1 \\ 4 \end{array}$

<i>Step 4</i>	<i>Step 5</i>
$\begin{array}{r} 3 \quad 9 \\ \swarrow \quad \searrow \\ 7 \quad 4 \\ \hline 3 \times 4 + 9 \times 7 = 75 \end{array}$	$\begin{array}{r} 3 \\ \downarrow \\ 7 \\ \hline 3 \times 7 = \\ 21 \end{array}$

<i>Step 3</i>	
$\begin{array}{r} 7 \quad 3 \quad 1 \\ \swarrow \quad \downarrow \quad \searrow \\ 6 \quad 8 \quad 2 \\ \hline 7 \times 2 + 3 \times 8 + 1 \times 6 = 44 \end{array}$	

Step 1: 30; 0 carry 3; $P_0 = 0$

Step 2: $74 + 3 = 77$; 7 carry 7; $P_1 = 7$

Step 3: $89 + 7 = 96$; 6 carry 9; $P_2 = 6$

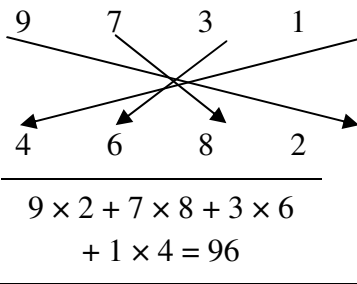
Step 4: $75 + 9 = 84$; 4 carry 8; $P_3 = 4$

Step 5: $21 + 8 = 29$; 9 carry 2; $P_4 = 9$

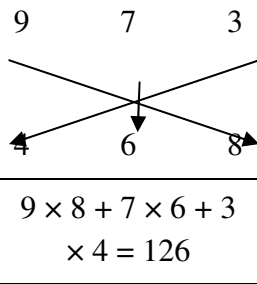
Carry of step 5 = $P_5 = 2$

Thus, the product is 294670.

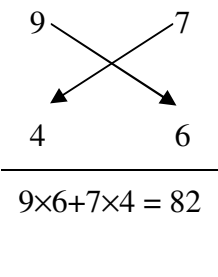
Step 4



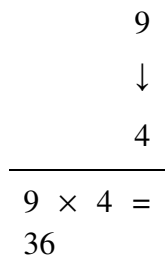
Step 5



Step 6



Step 7



- Step 1: 2; 2 carry 0; $P_0 = 2$
- Step 2: $14 + 0 = 14$; 4 carry 1; $P_1 = 4$
- Step 3: $44 + 1 = 45$; 5 carry 4; $P_2 = 5$
- Step 4: $96 + 4 = 100$; 0 carry 10; $P_3 = 0$
- Step 5: $126 + 10 = 136$; 6 carry 13; $P_4 = 6$
- Step 6: $82 + 13 = 95$; 5 carry 9; $P_5 = 5$
- Step 7: $36 + 9 = 45$; 5 carry 4; $P_6 = 5$
- Carry of step 7 = $P_7 = 4$

The product is 45560542.

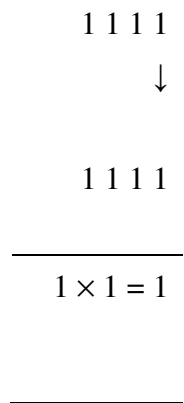
Similarly for the multiplication of two decimal numbers containing any number of digits, the above multiplication techniques can be applied.

3. Squaring of a Binary Number Using ‘Urdhva Tiryagbhyam’ Sutra

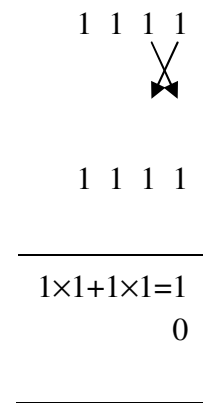
The method of multiplication using ‘Urdhva Tiryagbhyam’ sutra given in Section-2 can be implemented for squaring of a binary number and multiplication of two n - bit binary numbers. As an example, the squaring of 4-bit binary number 1111 is given below. The decimal equivalent of this number is 15.

Let $1111 \times 1111 = P_7P_6P_5P_4P_3P_2P_1P_0$

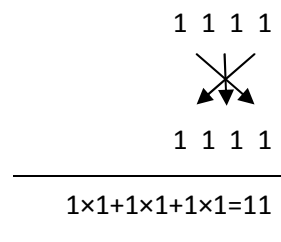
Step 1



Step 2



Step 3



is $P_7P_6P_5P_4P_3P_2P_1P_0$. C_1 to C_5 represent the carry from the previous product term.

Table 1. Method of squaring a 4-bit binary number.

Product term	Sum + Carry from previous term
P_0	a_0
P_1	$a_1 \times a_0 + a_1 \times a_0$
P_2	$a_2 \times a_0 + a_2 \times a_0 + a_1 + C_1$
P_3	$a_3 \times a_0 + a_3 \times a_0 + a_2 \times a_1 + a_2 \times a_1 + C_2$
P_4	$a_3 \times a_1 + a_3 \times a_1 + a_2 + C_3$
P_5	$a_3 \times a_2 + a_3 \times a_2 + C_4$
P_6	$a_3 + C_5$
P_7	Carry bit of P_6

The comparison between the number of multiplications (M) and additions (A) required in conventional and ‘Urdhva Tiryagbhyam’ method is shown in Table 2.

Table 2. Comparison between conventional method of multiplication and ‘Urdhva Tiryagbhyam’ method of multiplication.

Multiplication	Conventional Method		Urdhva Tiryagbhyam Method	
	M	A	M	A
2×2-bit multiplication	4	2	4	1

Step 4

$$\begin{array}{r}
 1\ 1\ 1\ 1 \\
 \times 1\ 1\ 1\ 1 \\
 \hline
 1 \times 1 + 1 \times 1 + 1 \times 1 + 1 \\
 \times 1 = 100
 \end{array}$$

Step 6

$$\begin{array}{r}
 1\ 1\ 1\ 1 \\
 \times 1\ 1\ 1\ 1 \\
 \hline
 1 \times 1 + 1 \times 1 = \\
 10
 \end{array}$$

Step 5

$$\begin{array}{r}
 1\ 1\ 1\ 1 \\
 \times 1\ 1\ 1\ 1 \\
 \hline
 1 \times 1 + 1 \times 1 + 1 \times 1 \\
 = 11
 \end{array}$$

Step 7

$$\begin{array}{r}
 1\ 1\ 1\ 1 \\
 \downarrow \\
 1\ 1\ 1\ 1 \\
 \hline
 1 \times 1 = 1
 \end{array}$$

- Step 1: 1; 1 carry 0; $P_0 = 1$
- Step 2: $10 + 0 = 10$; 0 carry 1; $P_1 = 0$
- Step 3: $11 + 1 = 100$; 0 carry 10; $P_2 = 0$
- Step 4: $100 + 10 = 110$; 0 carry 11; $P_3 = 0$
- Step 5: $11 + 11 = 110$; 0 carry 11; $P_4 = 0$
- Step 6: $10 + 11 = 101$; 1 carry 10; $P_5 = 1$
- Step 7: $1 + 10 = 11$; 1 carry 1; $P_6 = 1$
- Carry of step 7 = $P_7 = 1$

Thus, the square of 1111 is 11100001, whose decimal equivalent is $225 = 15^2$.

The general method of squaring of a 4-bit binary number $a_3a_2a_1a_0$ is illustrated in Table 1. The square operation $a_3a_2a_1a_0 \times a_3a_2a_1a_0$ will be of 8-bits long. Let the product term in 8-bits

3×3-bit multiplication	9	7	9	4
4×4-bit multiplication	16	15	16	9

4. Multiplier Based on ‘Urdhva Tiryagbhyam’ Sutra for Squaring 2-Bit Binary Number

A multiplier is one of the key hardware blocks in most of the digital signal processing systems. The hardware implementation of 2×2 bit multiplier using the concept of ‘Urdhva Tiryagbhyam’ sutra is shown in Fig.1. Let the product of two 2-bit binary numbers a_1a_0 and b_1b_0 is $P_3P_2P_1P_0$. It consists of four AND gates and two half adders. A half adder is a logic circuit that adds two binary digits and produces a 2-bit data, i.e., sum and carry. The 1st half adder is used to add a_1b_0 and a_0b_1 , the outputs of the 2nd and 3rd AND gates respectively. The 2nd half adder is used to add the carry c_1 generated from 1st half adder and the output a_1b_1 of the 4th AND gate. The output of 1st AND gate is P_0 . The sum of 1st half adder is P_1 and the sum of 2nd half adder is P_2 . The carry of 2nd half adder gives P_3 . The same architecture can be used for squaring a 2-bit binary number.

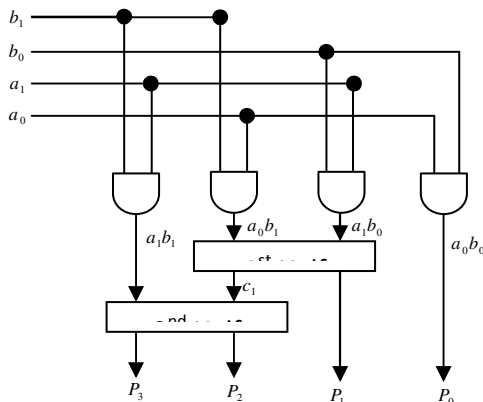


Figure 1. Block diagram of 2×2-bit multiplier based on ‘Urdhva Tiryagbhyam’ sutra.

5. Cubing of a Decimal Number Using ‘Anurupyena’ Sub-Sutra

The cubing operation using ‘Anurupyena’ sub-sutra is much better than the conventional cubing. According to this sub-sutra,

$$(ab)^3 = a^3 + 3ba^2 + 3ab^2 + b^3 \tag{1}$$

where a and b are the digits of a decimal number. Here (+) does not indicate ordinary addition. Two examples are given below for finding the cube of a decimal number using this sub-sutra.

Example 1: Consider a two digit decimal number 32. The cube of this number can be found out as per the following steps.

Step 1: Let $a = 3$ and $b = 2$

Step 2: Applying the ‘Anurupyena’ sub-sutra (1),

$$(32)^3 = 3^3 + 3 \times 2 \times 3^2 + 3 \times 3 \times 2^2 + 2^3$$

Step 3: Add the partial products in *Step 2* from right by shifting them one digit, as b contains one digit.

b^3	$= 2^3$	$=$	8
$+ 3ab^2$	$= 3 \times 3 \times 2^2$	$=$	36
$+ 3ba^2$	$= 3 \times 2 \times 3^2$	$=$	54
$+ a^3$	$= 3^3$	$=$	27
$(ab)^3$	$= 32^3$	$=$	32768

Example 2: The cube of the decimal number 423 can be calculated as given below.

Step 1: Let $a = 4$ and $b = 23$

Step 2: According to the sub-sutra (1),

$$423^3 = 4^3 + 3 \times 23 \times 4^2 + 3 \times 4 \times 23^2 + 23^3$$

Step 3: Add the partial products in Step 2 from right by shifting them by two digits, as b contains 2 digits.

$$\begin{array}{r} 23^3 = 12167 \\ + 3 \times 4 \times 23^2 = 6348 \\ + 3 \times 23 \times 4^2 = 1104 \\ + 4^3 = 64 \\ \hline \end{array}$$

$$(ab)^3 = 423^3 = 75686967$$

6. Cubing of a Binary Number Using ‘Anurupyena’ Sub-Sutra

The method of cubing a decimal number given in Section-5 can be applied for cubing a binary number. Two examples are given below for finding the cube of a binary number using the ‘Anurupyena’ sub-sutra.

Example 1: Let us consider the 3-bit binary number 101, whose decimal equivalent is 5. The cubing of this binary number is done by the following steps.

Step 1: Let $a = 10$ and $b = 1$

Step 2: According to the ‘Anurupyena’ sub-sutra (1),

$$(ab)^3 = (101)^3 = (10)^3 + 11 \times 1 \times (10)^2 + 11 \times 10 \times 1^2 + 1^3$$

Instead of 3 in the formula, its binary equivalent 11 shall be taken while adding the partial products.

Step 3: Add the partial products in Step 2 from right by shifting them by one bit, as b contains one bit.

$$\begin{array}{r} b^3 = 1^3 = 1 \\ + 3ab^2 = 11 \times 10 \times 1^2 = 110 \\ + 3ba^2 = 11 \times 1 \times (10)^2 = 1100 \\ + a^3 = (10)^3 = 1000 \\ \hline \end{array}$$

$$(ab)^3 = (101)^3 = 1111101$$

The decimal equivalent of 1111101 is $125 = 5^3$.

Example 2: Let us consider a 4-bit binary number 1001, whose decimal equivalent is 9. The cubing of 1001 is done as per the following steps.

Step 1: Let $a = 10$ and $b = 01$.

Step 2: Using the ‘Anurupyena’ sub-sutra (1),

$$(ab)^3 = (1001)^3 = (10)^3 + 11 \times 01 \times (10)^2 + 11 \times 10 \times (01)^2 + (01)^3$$

Step 3: Add the partial products in Step 2 from right by shifting them by 2 bits, as b contains 2 bits.

$$\begin{array}{r} b^3 = 01 \times 01 \times 01 = 0001 \\ + 3ab^2 = 11 \times 10 \times 01 \times 01 = 00110 \\ + 3ba^2 = 11 \times 01 \times 10 \times 10 = 01100 \\ + a^3 = 10 \times 10 \times 10 = 1000 \\ \hline \end{array}$$

$$(ab)^3 = (1001)^3 = 1011011001$$

The decimal equivalent of 1011011001 is $729 = 9^3$

References

[1] Bharati Krsna Tirthaji Maharaja, *Vedic Mathematics*, (Motilal Banarsidass Publishers Pvt.Ltd., Delhi, 2013).

- [2] H. D. Tiwari, G. Gankhuyag, C. M. Kim and Y. B. Cho, International SoC Design Conference (2008) II65-II68.
- [3] M. Ramalatha, K. Thanushkodi, K. Deena Dayalan and P. Dharani, International Conference on Advances in Recent Technologies in Communication and Computing, IEEE Computer Society (2009) 873- 875.
- [4] A. Havelia, International Journal of Technology And Engineering System, **2(1)** (2011) 27-31.
- [5] Prabha S. Kasliwal, B. P. Patil and D. K. Gautam, IETE Journal of Research, **57(1)** (2011) 39-41.
- [6] A. Ronisha Prakash and S. Kirubaveni, IEEE International Conference on Emerging Trends in Computing, Communication and Nanotechnology (2013) 89-94.

Physics Through Laboratory: Voltage Calibration Using Optical Method

Rashmi P.E.¹, ShivalingaSwamy T^{2*}, Raghu A.²

¹ Department of Physics,

Government College for Women,

Mandya-571401, INDIA.

² PG Department of Physics,

Government College (Autonomous),

Mandya-571401, INDIA.

*Corresponding author:tssphy@gmail.com

(Submitted: 11-08-2014)

Abstract

In this short article, we propose a simple, low cost and a novel optical method of calibrating DC motors and voltage sources by producing Lissajous-like spirograph patterns. Merits and limitations of the method are discussed. This experiment can be introduced to a 10+ course or to an undergraduate course with a modest budget.

1. Introduction

Low cost laser spirograph devices have been constructed earlier however they were used only to display the resultant patterns of light^[1,2]. In such setups, both DC motors and DC power supplies are essential part for their working. However, calibration of DC power supplies from such setups had not been studied so far. In this article we propose a simple procedure for the said calibration.

Laser beam position on the mirrors and hence the position of the image pattern (Spirograph) on the screen could be controlled by adjusting mirrors inclination. A simple spirograph could be made by attaching a pair of mirrors to the shafts of DC motors^[3,4].

A mathematical curve formed by combining two periodic vibrations at right angles to each other is called as a Lissajous figure. In an undergraduate lab these patterns were generally produced by feeding two signals from function generators to two channels of a CRO along X and Y. Technically, the patterns produced with the above set up may not be classified as Lissajous figures. First of all, there is only single beam involved in the process until the formation of final spirograph pattern and therefore the question of superposition of two waves were ruled out. However, the resultant spirograph describes similar variation in the final pattern as that exhibited by Lissajous pattern. Therefore here they are referred as the Lissajous – like figures.

Here the control parameters are the rotation speeds of DC motors. In this article, Lissajous-like figures are used for calibrating voltage of an unknown source with the help of a standard voltage source.

2. Image formation

A fine beam of laser from a laser pointer is shined on a spinning mirror that is attached to the shaft of a standard DC motor whose rotational speed is known. The reflected laser light will trace a circle on a projection surface and dependent on the speed of the motor being high enough, the laser path traced will appear to be a solid circle of variable frequency on the projection surface due to the persistence of vision. One can also consider it like a laser cone being reflected off of the rotating mirror. If we aim this reflected "laser cone" onto another rotating mirror, very interesting shapes begin to appear on the screen. The resultant shapes depends on the relative speed and hence on the applied voltage, of both the motors. When both mirrors are spinning, the circular patterns superimpose to produce such Lissajous like patterns. These patterns made to have integral number of loops, by adjusting the ratio of the two voltage sources to an integer. Further, since the speeds of the motors can be controlled by connecting the motors across variable voltage sources, voltage sources can be calibrated with the help of these Lissajous like figures^[5-8]. If one of the voltage sources is a standard one then the voltage of the other source can be estimated. Let ' n ' be the number of loops observed in the spirograph pattern when the voltage applied from the standard source is V_s . The voltage V of the power supply to be calibrated can be calculated using the relation

$$\frac{V}{V_s} = \frac{n}{1} \quad (1)$$

3. Experimental Setup

3.1 Materials used

Two identical DC motors with a voltage rating of 9V, two ordinary flat mirrors of 0.5 inch diameter, two variable DC power supplies of 0 – 5 V, a rheostat, a laser diode, true RMS digital multimeter and connecting wires.

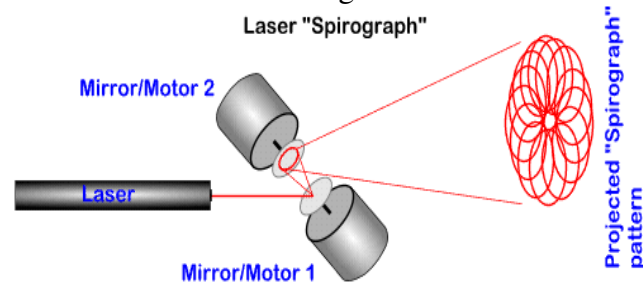


Figure 1: Schematics of experimental set up

3.2 Setup preparation

Initially, two flat mirrors each of 0.5 inch diameter were mounted at the ends of the DC motor shafts with the help of glue and allowed it dry completely. Then motors were mounted on wooden mounting brackets which are separated by short separation distance. These mounting brackets are arranged such that the mirrors face each other with some inclination and laser beam forms a Z-shaped path. The inclinations of motor/mirror assemblies can be tilted using adjustable screws to get patterns at a convenient position on the screen.

Then these DC motors were individually connected across two independent variable power supplies. Mirror /motor assembly were adjusted such that the circle of light from mirror 1 falls on mirror 2 and reflection from mirror 2 is projected onto the wall. Brilliant rotating spirograph patterns were observed as the voltages across the motor1 and 2 were varied.

3.3 Calibration of DC motors

In order to obtain only spirograph patterns two asynchronous DC motors are sufficient. On the other hand to carryout voltage calibrations using

these spirograph patterns two synchronous DC motors are necessary. To confirm this requirement the following procedure was used.

The workings of two mounted DC motors were tested independently by supplying suitable voltage to them.

In the setup, the voltage V_1 across one of the motors was kept at zero and the voltage V_2 across the other was varied in steps of 0.05V from the threshold voltage (0.45 V) to 0.65 V. The voltages from the power supply are measured from a true RMS digital multimeter. For each input, the time taken by the reflected spot of light to complete 20 rotations was noted for two trials and their average time ' t ' was determined. Then time period ' T ' and the frequency ' f ', of rotation of the DC motor were estimated from t and are tabulated in table 1. This study was limited to 0.65 V, as it was found difficult to trace the light spot at higher rotation speeds due to higher voltages. A plot of rotational frequency f of DC motor versus the applied voltage V_2 is drawn (see figure 2).

This procedure is repeated even for the second DC motor with the same power supply. The second DC motor was found to have same threshold voltage to start rotation.

Later, two mirrors were connected to the same power supply, one directly and the other through a rheostat, so that independent control of powering the two motors could be achieved. Input voltage was kept sufficiently above the DC motor threshold value. The voltage across second mirror was increased using the rheostat from 0. At certain voltage to the second DC motor a circular pattern was obtained, indicating the rotational speeds are equal. At even higher voltages, spectacular Lissajous like regular optical patterns were observed. They were correlated to the applied voltages.

For e.g.: when the voltage across motor 1 was 0.5 V and that across motor 2 was 1.5 V, then 3 loops were observed on the screen. The ratio of

the two voltages (1.5/0.5) gives 3, as expected for a Lissajous like pattern.

4. Calibration of an unknown power supply

Now, two motors are connected to two independent power supplies, one of them is used as a reference power supply. By keeping fixed voltage of 0.5V from the standard supply, we have varied the voltage from the other unknown source. When the voltage was increased from zero, we have observed a circular image on the screen. This is possible only when both the mirrors are spinning at the same speeds. Since identical DC motors are used in this work, the voltage delivered by the unknown power supply should be, now, exactly same as that of the reference source.

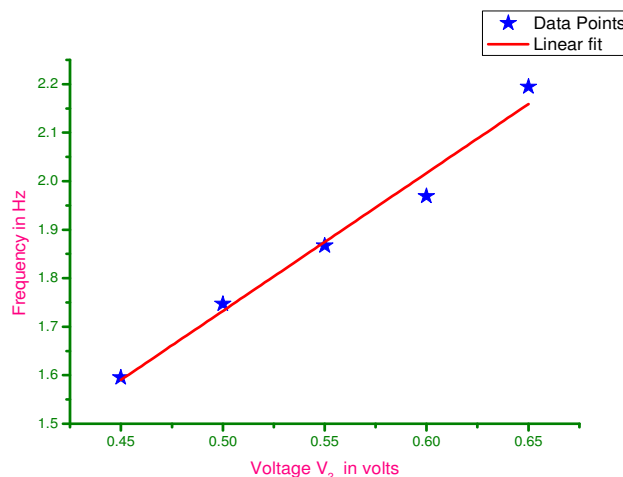


Figure 2: Calibration of one of the DC motor as a plot of f versus V .

The voltage across the second power supply was further increased until an integral number of regular loops were observed. The voltage of the power supply to be calibrated was estimated by the relation (1). These values were cross verified by measuring the voltage across the power supply using a digital Multimeter, when integral numbers of loops were observed.

5. Observations.

Table 1: Data showing relation between frequency of rotation of the pattern and the applied voltage

Voltage across the motors in V		Time for 20 rotations in s				Frequency of rotation f in s^{-1}
V_1	V_2	t_1	t_2	$t = (t_1 + t_2)/2$ $t = (t_1 + t_2)/2$	$\frac{T}{R}$ Period, $\frac{T}{R}$	
0	0.45	12.6	12.47	12.54	0.627	1.595
0	0.50	11.37	11.53	11.45	0.573	1.747
0	0.55	10.72	10.69	10.71	0.536	1.867
0	0.60	10.18	10.13	10.16	0.508	1.969
0	0.65	9.19	9.03	9.11	0.456	2.195

Calibration of voltage source:

Table 2: Data showing the voltage levels applied to DC Motors and number of loops found on the pattern.

Reference voltage, V in volts	No. of loops observed	Voltage V in volts	
		Calculated using (1)	Measured from DMM
0.5	1	0.5	0.5
0.5	2	1.0	1.0
0.5	3	1.5	1.5
0.5	4	2.0	2.0
0.5	5	2.5	2.5
0.5	6	3.0	3.0
0.5	7	3.5	3.5
0.5	8	4.0	4.0

6. Results and Discussions

The frequency of rotation of the spirograph pattern found to increase linearly with the applied voltage across the DC motor which serves to calibrate the DC motor. .

Main limitation of this method is that, only low voltages can be determined from this method as it becomes extremely difficult to notice the number of loops in the spirograph patterns at high voltages.

The voltage from the unknown power supply estimated using (1) as inferred by the spirograph

pattern found to match exactly with the value of the voltage measured using a digital multimeter. This serves to calibrate an unknown power supply.

7. Conclusions

This is an alternate inexpensive optical method for the calibration of low voltage sources and hence to determine the rotational speeds of DC motors. Further the experiment can be improved to obtain Lissajous-like patterns using AC power supplies and calibrate the AC power supplies.

References

- [1] Chris Chiaverina, The Physics Teacher **28**, 606 (1990); doi: 10.1119/1.2343177.
- [2] Keith Bellof, The Physics Teacher **42**, 504 (2004); doi: 10.1119/1.1814329.
- [3] <http://www.laserfx.com/Science/Science8.html> retrieved on 13-20-2014.
- [4] <http://www.exo.net>.
- [5] D., Christian A., et al. *Lombardi drawings of graphs Graph Drawing* (Springer Berlin Heidelberg, 2011).
- [6] Cundy, H. Martin and Rollett, A. P., *Mathematical Models*, (2nd. Ed., Oxford at the Clarendon Press 1961), pp. 242–253.
- [7] Franke, Herbert W., *Computer Graphics, Computer Art* (Phaidon 1971), pp. 60–64.
- [8] Herbert Gottlieb, “76. Applications, Lissajous patterns,” *Metrologic Laser Workbook and Catalog* (Metrologic Instruments, Bellmawr, NJ, 1987), p. 39.
-

The End